

Review

Hole Transport Materials for Tin-Based Perovskite Solar Cells: Properties, Progress, Prospects

Xinyao Chen ^{1,2}, Jin Cheng ^{2,*}, Linfeng He ², Longjiang Zhao ³, Chunqian Zhang ², Aiyong Pang ⁴
and Junming Li ² 

¹ School of Instrument Science and Opto Electronics Engineering, Beijing Information Science and Technology University, Beijing 100101, China; chenxinyao0206@163.com

² Beijing Key Laboratory for Sensor, School of Instrument Science and Opto-Electronics Engineering, Beijing Information Science and Technology University, Beijing 100101, China; zhangcq@bistu.edu.cn (C.Z.)

³ College of Engineering, Qufu Normal University, Rizhao 276826, China

⁴ Jiangsu Engineering Laboratory for Environmental Functional Materials, School of Chemistry and Chemical Engineering, Huaiyin Normal University, Huaian 223300, China

* Correspondence: chengjin@bistu.edu.cn

Abstract: The power conversion efficiency of modern perovskite solar cells has surpassed that of commercial photovoltaic technology, showing great potential for commercial applications. However, the current high-performance perovskite solar cells all contain toxic lead elements, blocking their progress toward industrialization. Lead-free tin-based perovskite solar cells have attracted tremendous research interest, and more than 14% power conversion efficiency has been achieved. In tin-based perovskite, Sn^{2+} is easily oxidized to Sn^{4+} in air. During this process, two additional electrons are introduced to form a heavy p-type doping perovskite layer, necessitating the production of hole transport materials different from that of lead-based perovskite devices or organic solar cells. In this review, for the first time, we summarize the hole transport materials used in the development of tin-based perovskite solar cells, describe the impact of different hole transport materials on the performance of tin-based perovskite solar cell devices, and summarize the recent progress of hole transport materials. Lastly, the development direction of lead-free tin-based perovskite devices in terms of hole transport materials is discussed based on their current development status. This comprehensive review contributes to the development of efficient, stable, and environmentally friendly tin-based perovskite devices and provides guidance for the hole transport layer material design.

Keywords: perovskite solar cell; tin-based; hole transport materials; energy level matching



Citation: Chen, X.; Cheng, J.; He, L.; Zhao, L.; Zhang, C.; Pang, A.; Li, J. Hole Transport Materials for Tin-Based Perovskite Solar Cells: Properties, Progress, Prospects. *Molecules* **2023**, *28*, 3787. <https://doi.org/10.3390/molecules28093787>

Academic Editors: Vilko Mandić, Ivana Panžić, Ivana Capan and Luka Pavić

Received: 23 March 2023

Revised: 9 April 2023

Accepted: 21 April 2023

Published: 28 April 2023



Copyright: © 2023 by the authors. Licensee MDPI, Basel, Switzerland. This article is an open access article distributed under the terms and conditions of the Creative Commons Attribution (CC BY) license (<https://creativecommons.org/licenses/by/4.0/>).

1. Introduction

In the face of the global energy crisis and environmental pollution, solar energy, as a renewable and clean energy source, is undoubtedly one of the most effective solutions. Moreover, by employing the photovoltaic effect, which converts solar energy into electricity, the solar energy approach presents as the most promising solution. At present, the main types of solar cells include inorganic semiconductor solar cells, organic semiconductor solar cells and perovskite solar cells. Perovskite solar cells, which use halide perovskite as the light-absorbing material, have received ample attention in the past decade. In 2009, Kojima et al. first introduced the perovskite structure of methylammonium lead iodide (MAPbI_3) and methylammonium lead bromide (MAPbBr_3) into dye-sensitized solar cells, achieving a photovoltaic conversion efficiency (PCE) of 3.8% [1]. In 2012, Nam-Gyu Park's group and Michael Grätzel's group collaborated to prepare the first all-solid-state perovskite solar cell with a cell efficiency of 9.7%; instead of liquid electrolyte, they utilized the solid-state hole-transport material 2,2',7,7'-tetrakis(N,N-di-p-methoxyphenyl-amine)9,9'-spirobifluorene (Spiro-OMeTAD) [2]. In the same year, an efficiency of 10.9% was achieved

by Henry J. Snaith's group; instead of TiO_2 , they utilized Al_2O_3 as the hole transport material with a mesoscopic structure [3]. After breaking through the 10% efficiency bottleneck, perovskite solar cells have been rapidly improved upon both in materials design and device fabrication technique. So far, the certified energy conversion efficiency (PCE) of perovskite solar cells is 25.7% [4], which already surpasses that of CdTe (22.1%), polycrystalline silicon (23.3%), and copper indium gallium selenide (23.4%) solar cells, making it one of the most intensive research topics in the field of solar cells [3,5–15]. Although perovskite solar cells have undergone extremely rapid development in recent years, there are still, however, many problems to be solved to realize the commercialization of perovskite solar cells. One of the most pressing issues is that the current high-performance perovskite solar cells all contain lead. Since the thermal and chemical stability of lead-based perovskite materials are relatively poor, most or all of the lead would be decomposed into the environment [16]. In particular, we found that these leaked lead ions enter the soil in a free state and they were absorbed by plants, and finally enter the food chain. Compared to the lead in the natural environment, the absorption capacity of plants for lead in perovskite materials is 10 times higher [17].

To replace the Pb ions with equivalent elements, the main B-metal elements that satisfy both the tolerance factor T and octahedral factor μ are tin (Sn), calcium (Ca), strontium (Sr), barium (Ba), bismuth (Bi) and tellurium (Te). In addition, it was found that when replacing Pb, the replaced element needs to hybridize effectively with the outer orbitals of the halogen group elements, to form the corresponding conduction and valence bands. Among these substitution materials, Sn has a similar shell electron configuration to Pb, a smaller ionic radius (Sn: 0.110 nm, Pb: 0.119 nm), a lower atomic mass and a higher 5s orbital energy level. Thus, the Sn-based perovskite has a similar energy level structure to Pb-based perovskite, with a band gap of about 1.30 eV, which is closer to the ideal band gap for solar cells than that of Pb-based perovskite. Meanwhile, tin-based perovskite materials have excellent photovoltaic properties such as high carrier mobility, high absorption coefficient in the visible region, and long exciton lifetime. The precise origin of these excellent optoelectronic properties is still largely unclear, and the fundamental understanding of charge migration processes will be important for further device optimization. One important point is that the migration properties of light-produced holes are determined by corresponding perovskite structures from the first-principles (ab initio) computations [18–20]. Thus, tin is one of the most likely alternatives to the lead-based perovskites [21,22]. However, the Sn^{2+} element is easily oxidized to Sn^{4+} under the presence of oxygen or water. Density function theory simulations suggest that the oxygen or water, by the formation of H-I or Sn-O bonds, would affect the Sn-I bonds in the tin perovskite, which is less significant in the case of lead perovskite [23]. In the PbX_2 for the lead perovskite, two electrons were donated from the Pb^{2+} cation 6p orbital to the p orbitals of two X^- anions [24].

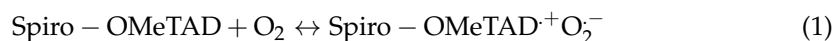
In 2014, Kanatzidis's group and Snaith's group almost simultaneously reported the first tin-based perovskite solar cells, with MASnBr_3 ($\text{MA}=\text{CH}_3\text{NH}_3$) or MASnI_3 as the active layer. The power conversion efficiency was around 6% [25,26]. However, the device reproducibility of these tin-based perovskite solar cells is low. Recently, the strategy of 2D-3D (quasi-2D) perovskite materials, which are 3D perovskite materials, doped with a small amount of 2D perovskite materials, has showed great potential for the development of efficient and stable tin-based perovskite cells. In quasi-2D perovskite solar cells, the amine molecules in 2D perovskite can coordinate with the organic cations in 3D perovskite, so that the 2D perovskite becomes implanted at the 3D perovskite crystal plane surface. It can effectively inhibit the non-radiative recombination at the grain boundaries and prevent the diffusion of water and oxygen into the internal 3D perovskite. In 2017, Liao et al. replaced the A-site ions FA^+ in the 3D perovskite material FASnI_3 ($\text{FA}=\text{CH}(\text{NH}_2)_2$) with large-size phenylethylammonium ions (PEA^+) for the first time; the original halogen octahedra expanding in the 3D direction to be isolated by these large-size ions, resulting in an increase in open-circuit voltage from 0.26 V undoped to 0.59 V, and the efficiency was increased to 6% [27]. Recently, Jiang et al. obtained a certified photovoltaic conversion efficiency of

14.6% by designing a new synthetic route that allows the fabrication of high-quality tin-perovskite films with fewer pinholes, more uniform orientation, and substantially increased carrier diffusion length [28]. Currently, the research focus has shifted from regular (n-i-p) to inverted (p-i-n) due to problems in the regular structure such as the diffusion length of holes being much shorter than that of electrons, the necessary chemical doping of hole transporting materials and the oxygen vacancies on the surface of titanium dioxide that accelerate Sn^{2+} oxidation. Meanwhile, the low open-circuit voltage is the main reason for the low performance of tin-based perovskite cells, thus now the main focus of research is on how to minimize the voltage loss, through the reduced defect density and the energy level alignment at the perovskite/charge transport layer interface.

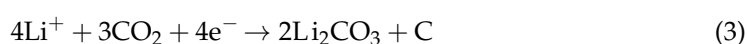
Recently, several reviews on tin-based perovskite material design and fabrication technique have been published. However, there were few reviews devoted to the hole transport layer. The hole transport layer, which is an important link in the structure of a perovskite solar cell for transporting holes and blocking electrons, has been well studied and selected for good performance in lead-based perovskite solar cells. Sn-X of Sn-based perovskites has a stronger s-p antibonding orbital than Pb-X, giving it a shallower conduction band and valence band position. In addition, the use of metal dopants should be avoided due to the instability of tin-based materials. This leads to the fact that the design experience of previous hole transport materials in lead-based perovskite solar cells and organic solar cells is not applicable to the tin-based perovskite devices, so it is necessary to summarize the study of hole transport materials in tin-based perovskite solar cells. In this work, we first summarize the current progress of tin-based perovskite solar cells using different hole transport materials, then describe the impact of different hole transport materials on the performance of tin-based devices, and finally discuss the direction of development of lead-free tin-based perovskite devices in terms of hole transport materials. This comprehensive review contributes to the environmentally friendly tin-based perovskite solar cell device structures and provides guidance for the realization of efficient and stable non-lead perovskite solar cells through material design.

2. Classical Hole Transport Layer: Spiro-OMeTAD

The initial introduction of tin-based perovskite solar cells has benefitted from the successful experiences gathered from lead-based perovskite solar cells. The most classic hole transport material in lead-based perovskite solar cells is Spiro-OMeTAD. In 2012, Spiro-OMeTAD was introduced for the first time to prepare the all-solid-state perovskite solar cell as the hole transport material [2]. Today, the highest efficiency of perovskite solar cells is 25.7%, also using Spiro-OMeTAD as the hole transport layer. Figure 1 summarizes the hole transport materials used for the highest efficiency of perovskite solar cells [2–4,29–37]. To obtain Spiro-OMeTAD films with high hole mobility and conductivity, typically three preparation processes are used: (1) addition of P-type dopants lithium bistrifluoromethanesulfonimide (Li-TFSI) and 4-tert-butylpyridine (tBP): Li-TFSI regulate the reaction of O_2 with Spiro-OMeTAD under illumination, and provide TFSI^- stable radical cations along with lithium oxides. Such an oxidation process relies on very slow oxygen entry in air and diffusion through Spiro-OMeTAD:Li-TFSI, as follows [26]:



(2) Addition of the strong oxidation dopant tris(2-(1H-pyrazol-1-yl)-4-tert-butylpyridine) cobalt (III) tris-(bis(tri-fluoromethane) sulfonimide) (FK209) to the Spiro-OMeTAD:LiTFSI:tBP solution, to replace the slow oxidation process; (3) exposure to UV light excitation for Spiro-OMeTAD:LiTFSI solution with CO_2 gas bubbling treatment, in which CO_2 gains electrons from photoexcited Spiro-OMeTAD to achieve p-doping [38,39], as follows:



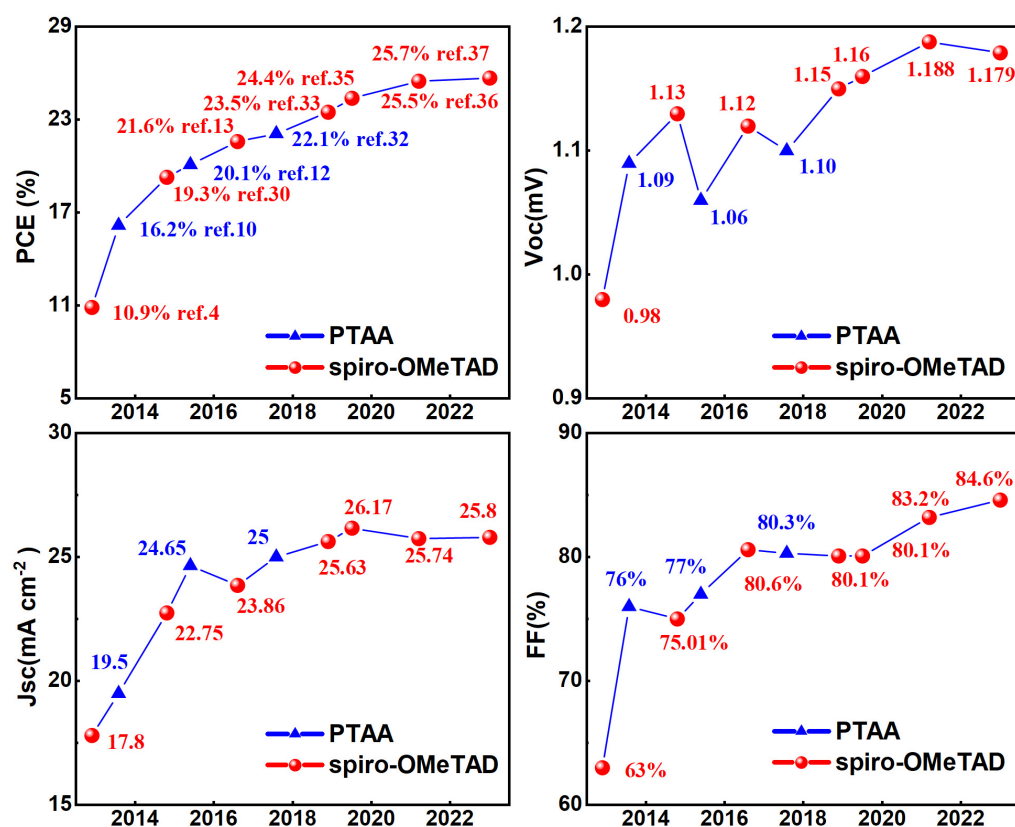


Figure 1. Performance of perovskite solar cells with recorded efficiency over the last decade [2–4,10,12,13,29–37].

2.1. Limitations of Pure Spiro-OMeTAD

Before copying the success of lead-based perovskite solar cells with Spiro-OMeTAD as the hole transport layer, the tin-based perovskite layer faces an inevitable problem: when exposed to acetonitrile solution of tBP:Li-TFSI, the hygroscopic properties of the lithium salt therein accelerate the oxidation of Sn^{2+} to Sn^{4+} ; thus, even with rapid cobalt doping processing, the degradation of the tin-based perovskite film cannot be avoided. When the undoped Spiro-OMeTAD was used as the hole transport layer, Wang et al., Kumar et al. and Ke et al. found that although from the perspective of tin-based perovskite films, undoped Spiro-OMeTAD fundamentally solved the problem of additive-induced film instability, respectively. However, in terms of overall device performance, undoped Spiro-OMeTAD could not achieve high conductivity without doping or oxidation, which limits the charge transport in the hole transport layer and thus limits the performance of the PV device ($\text{PCE} < 1\%$) (summarized in Table 1). Moreover, the energy levels of pure Spiro-OMeTAD were badly mismatched with the tin-based perovskite, which induced a low device voltage [40–42].

Table 1. Performance of tin-based perovskite solar cells based on Spiro-OMeTAD as hole transport layer.

Perovskite	Device Structure	Voc (mV)	Jsc (mA/cm ²)	FF (%)	PCE (%)	Ref.
B-γ-CsSnI ₃	ITO/TiO ₂ /PVSK/Spiro-OMeTAD/Au	480	8.11	19.80	0.77	[40]
en-FASnI ₃	FTO/c-TiO ₂ /mp-TiO ₂ /PVSK/Spiro-OMeTAD/Au	429	13.38	30.79	1.77	[41]
CsSnI ₃ + 20 mol%SnF ₂	FTO/c-TiO ₂ /mp-TiO ₂ /PVSK/Spiro-OMeTAD/Au	240	25.80	30.00	1.87	[42]
CsSnBr ₃	FTO/c-TiO ₂ /mp-TiO ₂ /PVSK/Spiro-OMeTAD + Li-TFSI + tBP/Au	410	9.00	58.00	2.10	[43]
FASnI ₃	FTO/TiO ₂ +PVSK/Spiro-OMeTAD + Li-TFSI + tBP/Au	238	24.45	36.00	2.10	[44]
MASnBr ₃	FTO/c-TiO ₂ /PVSK/Spiro-OMeTAD + Li-TFSI + tBP/Au	236	0.03	25.60	0.002	[45]
MASnI ₃	FTO/c-TiO ₂ /mp-TiO ₂ /PVSK/Spiro-OMeTAD + H-TFSI + tBP/Au	880	16.8	42.00	6.40	[25]
MASnI ₃	FTO/c-TiO ₂ /mp-TiO ₂ /PVSK/Spiro-OMeTAD + H-TFSI + 2,6-lutidine/Au	680	16.30	48.00	5.23	[26]
MASnI ₂ Br	FTO/c-TiO ₂ /mp-TiO ₂ /PVSK/Spiro-OMeTAD + H-TFSI + 2,6-lutidine/Au	770	14.38	50.00	5.48	[26]
MASnI ₂ Br ₂	FTO/c-TiO ₂ /mp-TiO ₂ /PVSK/Spiro-OMeTAD + H-TFSI + 2,6-lutidine/Au	820	12.30	57.00	5.73	[26]
MASnBr ₃	FTO/c-TiO ₂ /mp-TiO ₂ /PVSK/Spiro-OMeTAD + H-TFSI + 2,6-lutidine/Au	880	8.26	59.00	4.27	[26]
FASnI ₃ (25mol% Br)	FTO/c-TiO ₂ /mp-TiO ₂ /PVSK/Spiro-OMeTAD + H-TFSI + 2,6-lutidine/Au	414	19.80	66.90	5.50	[46]

2.2. Doping of Spiro-OMeTAD

2.2.1. Spiro-OMeTAD + Li-TFSI + tBP

Gupta et al. explored an all-inorganic tin-based perovskite photovoltaic device with Spiro-OMeTAD as the hole transport material and SnF₂-doped cesium bromide tin (CsSnBr₃) as the light absorbing layer. The device structure was FTO/d-TiO₂/mp-TiO₂/Perovskite/Spiro-OMeTAD/Au (Figure 2c) [43]. In their work, the Spiro-OMeTAD layer was prepared by adding 75 mg of Spiro-OMeTAD in 1 mL of chlorobenzene; followed by adding tBP and Li-TFSI to the solution to improve the conductivity by doping with tBP and Li-TFSI. Under simulated 100 mW/cm² AM 1.5G irradiation, the device showed a power conversion efficiency of 2.10%, a short-circuit current of 9 mA/cm², an open-circuit voltage of 410 mV and a fill factor of 58% (Table 1). In their work, 20 mol% SnF₂ was doped in the light absorption layer. Figure 2a,b show the current density–voltage curves of the device (with/without SnF₂) in the dark and under light, and it can be observed that the photovoltaic conversion efficiency is significantly improved by a factor of 200 with SnF₂ doping. The addition of SnF₂ dopant reduced the work function of CsSnBr₃ (WF = 4.52 eV and $E_{\text{VBM}} = -6.10$ eV) and greatly lowered the ionization potential compared to the original CsSnBr₃ (WF = 4.62 eV) and ($E_{\text{VBM}} = -6.33$ eV). The doping of Li-TFSI brings the highest occupied molecular orbital (HOMO) of the hole transport layer close to the EVBM of the perovskite (closer than that of pure spiro-OMeTAD), improving the energy level alignment between the tin-based perovskite layer and the hole transport layer, which in turn reduces the large voltage loss at the HTM/Perovskite interface (Figure 2d). The authors also point out that this conclusion needs further investigation. However, the lithium salts could bleach the perovskite film during the spiro-OMeTAD drop-casting process.

In summary, the conventional preparation methods of Spiro-OMeTAD and Li-TFSI present two main issues: First, the tin-based perovskite films were sensitive when exposed to acetonitrile solutions with tBP and Li-TFSI. The hygroscopic properties of the lithium salt in the Spiro-OMeTAD layer would accelerate the oxidation of Sn²⁺ to Sn⁴⁺, resulting in a sharp decrease in device performance. During the spin-coating of tBP:acetonitrile-doped Spiro-OMeTAD solution, the degradation of the tin-based perovskite film is unavoidable even with fast processing [41,43–45]. Chlorobenzene as a solvent alone or chlorobenzene with Spiro-OMeTAD:tBP does not change the color of the perovskite film; however, it may form a highly resistant interfacial phase after Spiro-OMeTAD deposition. The solar cells prepared by this method exhibit high-resistance characteristics, which would lead to a high voltage loss and consequently reduced fill factor [41]. Second, to achieve the champion performance of Spiro-OMeTAD, Li-TFSI is required to mediate the reaction of O₂ with Spiro-OMeTAD in the presence of light to produce TFSI-stabilized radical cations with the lithium oxide to complete the doping. Such an oxidation process relies on the very slow entry and diffusion of oxygen through Spiro-OMeTAD:Li-TFSI; on the other hand, the tin-based perovskite film was extremely air-sensitive, which contrasted exactly against the oxidation process of Spiro-OMeTAD:Li-TFSI. The stability of encapsulated tin-based

devices prepared using Spiro-OMeTAD:Li-TFSI:tBP as the hole transport layer was also relatively poor [39].

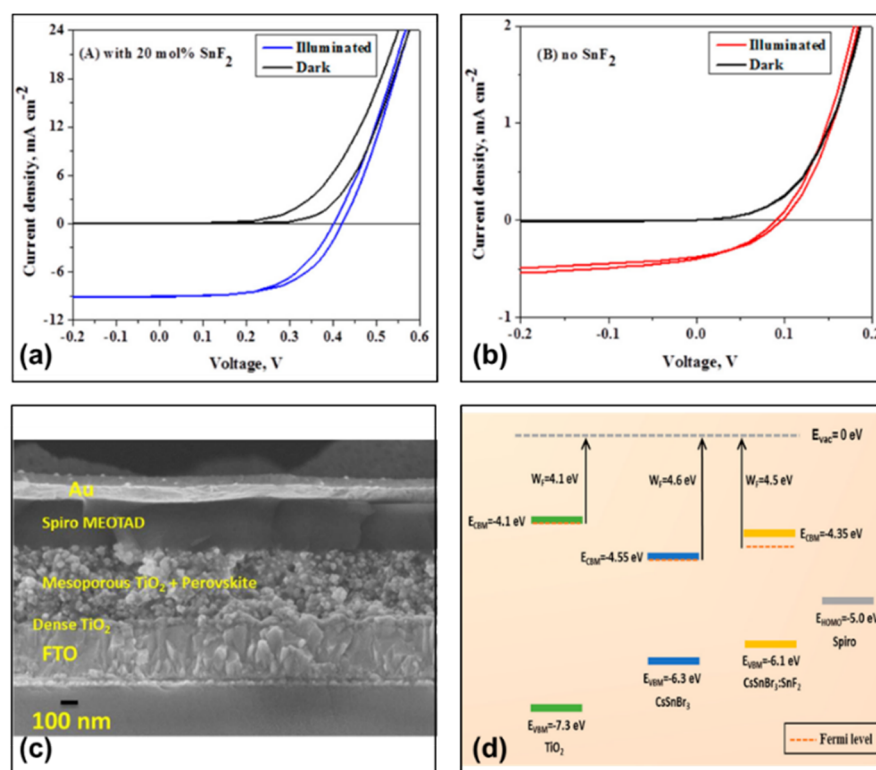


Figure 2. Current density–Voltage characteristics of the champion CsSnBr₃ device (a) with SnF₂ and (b) without SnF₂ devices under dark and light conditions. (c) Cross-section scanning electron microscopy (SEM) image of CsSnBr₃ devices. (d) Valence band maximum, conduction band minimum and Fermi energy levels of dense TiO₂, CsSnBr₃ and CsSnBr₃ (with 20 mol% SnF₂) materials [43]. Reprinted with permission from Ref. [42]. Copyright 2016 American Chemical Society.

2.2.2. Spiro-OMeTAD + H-TFSI + tBP

To solve the problem whereby the hygroscopic property of lithium salts accelerates the oxidation of Sn²⁺ to Sn⁴⁺, Noel et al. used hydrogen bis(tri-fluoromethanesulfonyl) imide (H-TFSI) to replace Li-TFSI. With MASnI₃ as the absorbing layer, they prepared FTO/c-TiO₂/mp-TiO₂/MASnI₃/Spiro-OMeTAD/Au structure solar cells (Figure 3a) [25]. The formulation of the hole transport layer was 80 mM Spiro-OMeTAD, 10 mM H-TFSI and 80 mM tBP. The device obtained a photovoltaic conversion efficiency of 6.40%, an open-circuit voltage of 880 mV, a short-circuit current density of 16.80 mA/cm² and 42% fill factor (Figure 3b, Table 1). The cell performance parameters using tin-based MASnI₃ and lead-based (MAPbI_{3-x}Cl_x) as light absorber layer are shown in Figure 3c. The replacement of Li-TFSI by H-TFSI can partially solve the problem of the hygroscopic properties of lithium salts causing an acceleration in the oxidation of Sn²⁺ to Sn⁴⁺. However, another additive in the precursor solution of the cavity transport layer, tBP, can react with MASnI₃ and form colorless coordination complexes or hydroxides. In addition, tBP, as a strong alkali, can also damage the film when used in large amounts or over a long period of time [47].

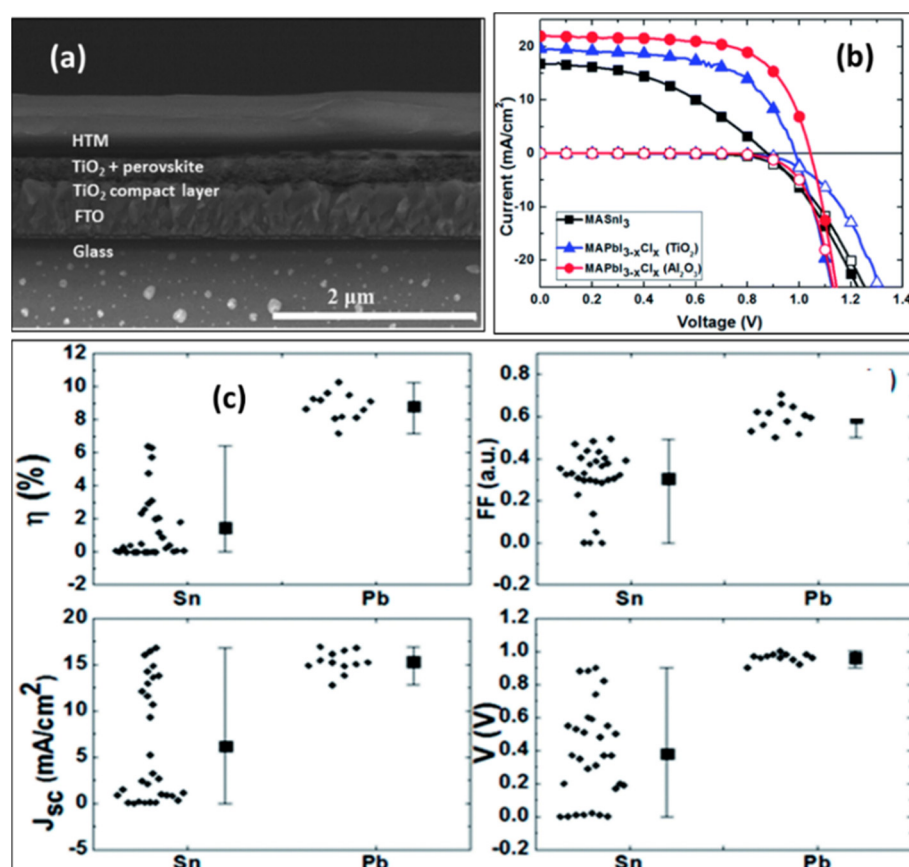


Figure 3. (a) Cross-sectional SEM image of the device with FTO/c-TiO₂ (50 nm)/mp-TiO₂/MASnI₃ (400 nm)/Spiro-OMeTAD (doped, 600 nm)/Au. (b) Performance of the champion tin-based and lead-based perovskite solar cells from the same batch, with the bright current curves indicated by solid symbols and dark current curves shown with hollow symbols. (c) Current–voltage characteristics and device performance parameters for power conversion efficiency, fill factor, short-circuit current and open-circuit voltage, respectively. The device performance data are shown on the left side of the figure for tin-based MASnI₃ and on the right side for lead-based MAPbI_{3-x}Cl_x for light-absorbing materials [25]. Reprinted with permission from Ref. [21]. Copyright 2014 The Royal Society of Chemistry.

2.2.3. Spiro-OMeTAD + H-TFSI + 2,6-lutidine

In 2014, Hao et al. utilized MASnI_{3-x}Br_x as the light absorbing layer and Spiro-OMeTAD with 2,6-lutidine replacement of tBP material (to enhance the hole mobility) as the hole transport layer, and prepared tin-based perovskite solar cells with device structure of FTO/c-TiO₂/mp-TiO₂/Perovskite/Spiro-OMeTAD/Au (Figure 4a) [26]. In this case, the preparation of the hole transport layer Spiro-OMeTAD was obtained from 72.3 mg of Spiro-OMeTAD, 30 mL of 2,6-lutidine, 17.5 μ L of acetonitrile solution of Li-TFSI (concentration of 520 mg mL⁻¹), dissolved in 1 mL of chlorobenzene solution. For the MASnI_{3-x}Br_x perovskites, the conduction band changed from 4.17 eV for MASnI₃, 3.96 eV for MASnI₂Br, 3.78 eV for MASnIBr₂, and 3.39 eV for MASnBr₃. From the energy band alignment diagram, the change in the band gap (E_g) of MASnI_{3-x}Br_x is mainly due to the shift of the conduction band to an upper position. These energy level changes allow for band gap engineering and energetics tuning to achieve more efficient solar cell structures (Figure 4b). Ultimately, the device based on the MASnIBr₂ obtained a maximum efficiency of 5.70%, corresponding to a short-circuit current of 12.30 mA/cm², an open-circuit voltage of 820 mV and a fill factor of 57% (Figure 4c, Table 1). However, the 2,6-lutidine remained a base, and thus would damage the tin perovskite film over long time periods.

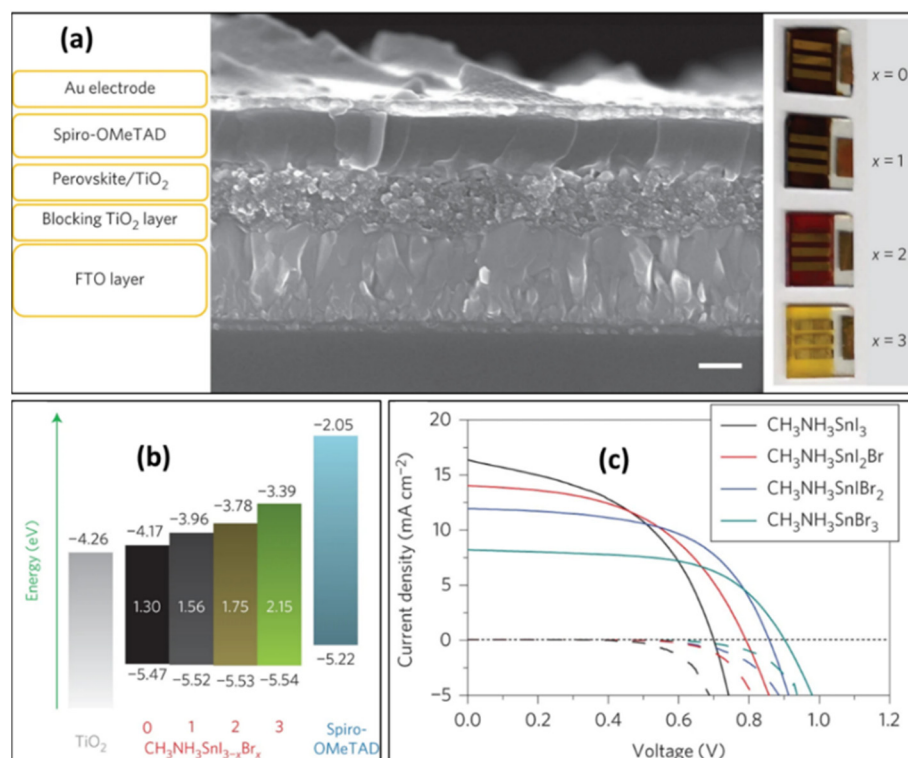


Figure 4. (a) SEM image of a tin-based perovskite solar cell with MASnI₃ as the light absorbing layer; the structure of the device is FTO/c-TiO₂/mp-TiO₂/Perovskite/Spiro-OMeTAD/Au, and the real device image on the right side showing the color of the photovoltaic device made from MASnI_{3-x}Br_x. (b) Schematic of the energy level structure of a tin-based perovskite photovoltaic device; (c) Current–voltage diagram of tin-based photovoltaic device under one sunlight irradiation, MASnI₃, MASnI₂Br, MASnIBr₂ and MASnBr₃, respectively [26]. Reprinted with permission from Ref. [22]. Copyright 2014 Springer Nature.

In 2017, Lee et al. in the preparation of Spiro-OMeTAD hole transport layer, they also replaced the tBP material with 2,6-lutidine. The device's structure was FTO/c-TiO₂/mp-TiO₂/Perovskite/Spiro-OMeTAD/Au, with TiO₂ as the electron transport layer and Br-doped (25 mol%) FASnI₃ as the light-absorbing layer (Figure 5a) [46]. The precursor solution for the hole transport layer contained Spiro-OMeTAD/chlorobenzene (72.3 mg/mL, 1 mL) solution, 17.5 μ L of H-TFSI/acetonitrile (509 mg/mL) solution and 30 μ L of 2,6-lutidine. Br doping in FASnI₃ significantly reduced the carrier density of the perovskite absorber (Figure 5a) and its interaction with the TiO₂ electron energy levels of the transport layer were better matched (Figure 5b). The optimal cell device achieved a photovoltaic conversion efficiency of 5.50%, corresponding to a short-circuit current density of 19.80 mA/cm², an open-circuit voltage of 414 mV, and a fill factor of 66.90% (Figure 5c, Table 1). In a 100-s maximum power point tracking measurement, the steady-state current density was 17.0 mA/cm² and the stable power conversion efficiency was 5% (Figure 5d). Although the film color remained constant when 2,6-lutidine was used. However, since 2,6-lutidine itself is an alkali, it can still damage the film when used in a large amount or for a long period of time.

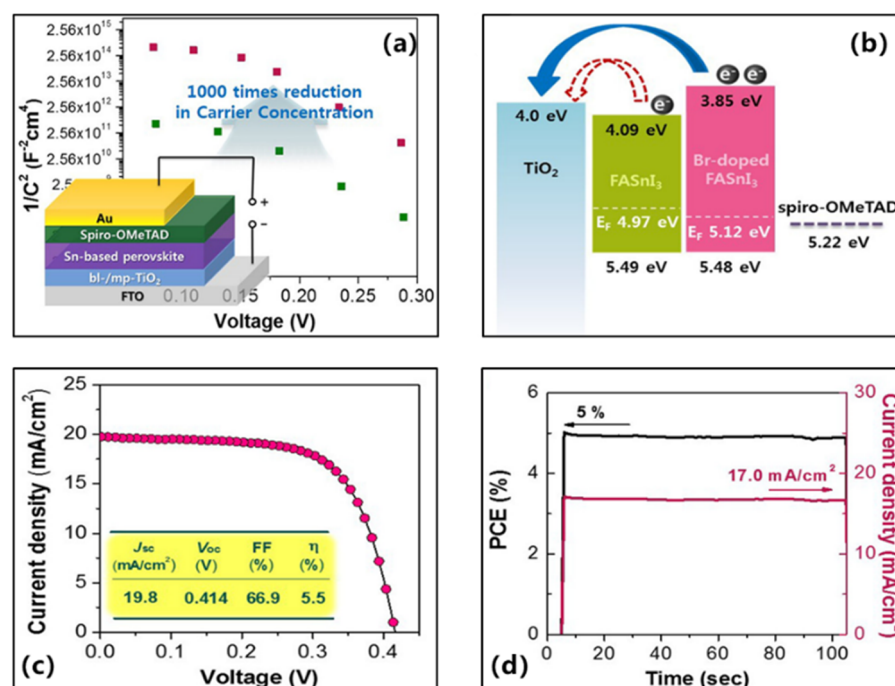


Figure 5. (a) Device diagram of FASnI₃-based perovskite solar cell. (b) Energy schematics of TiO₂, FASnI₃ and Br-doped FASnI₃ films. (c) The density–voltage curves of champion devices under reverse scan. (d) Stable efficiency and current–voltage curve of champion device measured at 293 mV voltage for 100s [46]. Reprinted with permission from Ref. [46]. Copyright 2018 American Chemical Society.

In summary, although efforts have been made to improve the performance of tin-based perovskite solar cell devices based on Spiro-OMeTAD layers, it is still challenging to obtain high-performance devices. This is because the use of dopants, whether tBP, or LiTFSi, or 2,6-lutidine always destroys the tin-based perovskite film; thus, the doped Spiro-OMeTAD cannot achieve high performance. Lessons could be learned from the improvement of electrical properties of Spiro-OMeTAD in Pb-based perovskite solar cells, such as organic Lewis acid [48]. In addition, based on this orthotropic structure of tin-based perovskite solar cells, there are also many laboratories that have conducted studies targeting Poly bis(4-phenyl)(2,4,6-trimethylphenyl) amine (PTAA), poly 3-hexylthiophene (P3HT), four tetraphenylethylene (TPE), and other hole transport materials.

3. Replacement of Organic Materials for Spiro-OMeTAD

3.1. Organic PTAA

3.1.1. PTAA + LiTFSI + tBP

In 2020, Li et al. utilized 2D tin-based Ruddlesden-Popper (R-P) phase perovskites of A₂(FA)_{n-1}SnnI_{3n+1} (A = BA = CH₃(CH₂)₃NH₃⁺, or = OA = CH₃(CH₂)₇NH₃⁺, or = DA = CH₃(CH₂)₁₁NH₃⁺) as the light-absorbing layer, and utilized PTAA as the hole transport material to fabricate the perovskite solar cells (FTO/c-TiO₂/mp-TiO₂/BA-PVSK/PTAA/Au) [49]. The PTAA precursor solution consisted of 10 mg of PTAA, 10 μ L of Li-TFSI in acetonitrile (170 mg/mL) and 5 μ L of tBP in 1 mL of toluene solution. Ultimately, the device obtained a power conversion efficiency of 4%, a short-circuit current of 24 mA/cm², an open-circuit voltage of 420 mV, a fill factor of 40.20% (Figure 6a,b, Table 2) and a higher average PCE relative to the organic spacer cations with different chain lengths (Figure 6c). The effect of the organic spacer cations with different chain length on the crystal orientation and phase distribution of perovskite films was investigated. An increase in chain length would decrease the Fermi energy level E_F , and the valance band maximum of these 2D perovskite were estimated as 5.04 eV for BA, 5.04 eV for OA, and 5.06 eV for DA, which were well matched with the PTAA hole transport layer (5.1 eV) (Figure 6d). The

organic spacer cations with shorter alkyl chain lengths (e.g., BA) would promote vertical crystal growth of perovskite films, which could reduce Sn^{2+} oxidation and improved charge carrier transport.

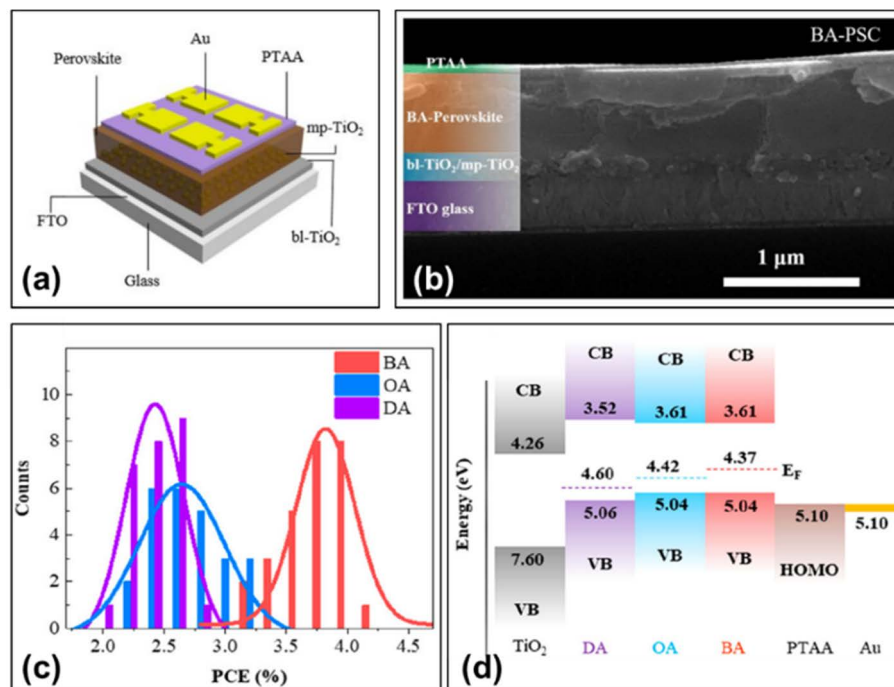


Figure 6. (a) Device diagram based on BA-perovskite thin film; (b) cross-sectional SEM image of 2D/3D perovskite solar cells; (c) PCE histogram of 2D/3D perovskite solar cells with 20 samples. (d) Schematic diagram of the energy level structure of 2D/3D perovskite solar cells [49]. Reprinted with permission from Ref. [47]. Copyright 2020 American Chemical Society.

Table 2. Performance parameters of tin-based perovskite solar cells based on organic materials as hole transport layer.

Perovskite	Device Structure	Voc (mV)	Jsc (mA/cm ²)	FF (%)	PCE (%)	Ref.
BA ₂ (FA) _{n-1} SnI _{3n+1}	FTO/c-TiO ₂ /mp-TiO ₂ /BA-PVSK/PTAA + Li-TFSI + tBP/Au	420	23.98	40.21	4.04	[49]
OA ₂ (FA) _{n-1} SnI _{3n+1}	FTO/c-TiO ₂ /mp-TiO ₂ /OA-PVSK/PTAA + Li-TFSI + tBP/Au	391	20.21	37.84	2.99	[49]
DA ₂ (FA) _{n-1} SnI _{3n+1}	FTO/c-TiO ₂ /mp-TiO ₂ /DA-PVSK/PTAA + Li-TFSI + tBP/Au	325	16.48	44.95	2.41	[49]
MASnI ₃	FTO/c-TiO ₂ /mp-TiO ₂ /PVSK/PTAA + Li-TFSI + tBP/Au	300	26.10	30.00	1.90	[50]
MASnI ₃	FTO/c-TiO ₂ /mp-TiO ₂ /PVSK/PTAA + Li-TFSI + tBP/Au	230	26.00	39.00	2.30	[51]
FASnI ₃	FTO/c-TiO ₂ /mp-TiO ₂ /PVSK/PTAA + TPFB/Au	380	23.09	60.00	5.27	[52]
en-FASnI ₃	FTO/c-TiO ₂ /mp-TiO ₂ /PVSK/PTAA + TPFB/Au	480	22.54	65.96	7.14	[53]
MASnI ₃	FTO/c-TiO ₂ /mp-TiO ₂ /PVSK/PTAA + TPFB/Au	273	17.80	39.00	1.86	[47]
(BA) ₂ MA ₃ Sn ₄ I ₁₃	FTO/c-TiO ₂ /mp-TiO ₂ /infiltrated PVSK/PVSK capping layer/PTAA + TPFB/Au	229	24.10	45.70	2.53	[54]
en-MASnI ₃	FTO/c-TiO ₂ /mp-TiO ₂ /PVSK/PTAA + TPFB/Au	428	24.28	63.72	6.63	[55]
MASnI ₃	FTO/c-TiO ₂ /mp-TiO ₂ /PVSK/PVSK/PTAA + TPFB/Au	378	19.92	51.73	3.89	[56]
FASnI ₃ (10%PN)	FTO/c-TiO ₂ /mp-TiO ₂ /PVSK/PTAA + TPFB/Au	435	22.15	60.67	5.85	[57]
en-FASnI ₃	FTO/SnO ₂ -CPTA/PVSK/PTAA + TPFB/Au	720	16.45	65.00	7.40	[58]
MASnBr ₃	FTO/c-TiO ₂ /PVSK/P3HT/Au	498	4.27	49.10	1.12	[45]
Cs ₂ SnI ₆	FTO/c-ZnO/n-ZnO/PVSK/P3HT/Ag	520	3.20	51.50	1.00	[59]
Cs ₂ SnI ₆	FTO/TiO ₂ /PVSK/P3HT/Ag	510	5.41	35.00	1.00	[60]
en-FASnI ₃	FTO/c-TiO ₂ /mp-TiO ₂ /en-FASnI ₃ /TPE/Au	453	22.60	67.00	6.85	[41]

Table 2. Cont.

Perovskite	Device Structure	Voc (mV)	Jsc (mA/cm ²)	FF (%)	PCE (%)	Ref.
FASnI ₃ (10mol%SnF ₂)	ITO/PEDOT:PSS/PVSK/C60/BCP/Ag	465	22.07	60.00	6.22	[61]
MASnI ₃ (LT-Mix)	ITO/PEDOT:PSS/MASnI ₃ /C60/BCP/Ag	450	11.82	40.00	2.14	[62]
PP-FASnI ₃	ITO/PEDOT:PSS/PP-FASnI ₃ /C60/BCP/Ag	330	17.78	67.9	3.98	[63]
(FA) _{0.75} (MA) _{0.25} SnI ₃	ITO/PEDOT:PSS/PVSK/C60/BCP/Ag	610	21.20	62.70	8.12	[64]
FASnI ₃	ITO/PEDOT:PSS/FASnI ₃ /C60/BCP/Cu	450	24.87	63.00	7.05	[65]
FASnI ₃ :PMMA	ITO/PEDOT:PSS/FASnI ₃ :PMMA/PCBM/Ag	482	13.17	57.00	3.62	[66]
FASnI ₃ (2.5%N ₂ H ₅ Cl)	ITO/PEDOT:PSS/FASnI ₃ /PCBM/BCP/Ag	455	17.63	67.30	5.40	[67]
(PEAI) _{0.1} FA _{0.9} SnI ₃ (5%FASCN)	ITO/PEDOT:PSS/PVSK/PCBM/Al	530	21.80	66.50	7.66	[68]
(PEAI) _{0.08} FA _{0.92} SnI ₃	ITO/PEDOT:PSS/PVSK/C60/BCP/Al	525	24.10	71.00	9.00	[69]
FASnI ₃ + SnF ₂ + TMA	ITO/PEDOT:PSS/FASnI ₃ /C60:1 wt% TBAI/Ag	470	22.45	67.80	7.09	[70]
GA _x FA _(0.98-x) SnI ₃ -1% EDAl ₂	ITO/PEDOT:PSS/PVSK/C60/BCP/Ag	619	21.20	72.90	9.60	[71]
FA _{0.98} EDA _{0.01} SnI ₃ (0.05 mM DAE)	FTO/PEDOT:PSS/PVSK/C60/BCP/Ag/Au	600	23.09	73.00	10.18	[72]
FASnI ₃ (3%5-AVAI)	ITO/PEDOT:PSS/FASnI ₃ /PCBM/BCP/Ag	592	18.89	62.30	7.00	[73]
FASnI ₃ (PEABr)	ITO/PEDOT:PSS/PVSK/PCBM/BCP/Al/Ag	540	22.64	64.00	7.86	[74]
EA _{0.1} (FA _{0.75} MA _{0.25}) _{0.9} SnI ₃	ITO/PEDOT:PSS/PVSK/PCBM/C60/BCP/Ag/Au	470	17.45	66.00	5.41	[75]
(BA _{0.5} PEA _{0.5}) ₂ FA ₂ Sn ₄ I ₁₃	ITO/PEDOT:PSS/PVSK/C60/LiF/Al	600	21.82	66.73	8.82	[76]
FASnI ₃ (15%PPAI)	ITO/PEDOT:PSS/PVSK/C60/BCP/Ag	560	23.22	72.60	9.44	[77]
EA _{0.08} -FASnI ₃ /PEA ₂ FASn ₂ I ₇	ITO/PEDOT:PSS/PVSK/C60/BCP/Al	510	23.75	70.00	8.40	[78]
AVA ₂ FA _{n-1} Sn _n I _{3n+1} (10%NH ₄ Cl)	ITO/PEDOT:PSS/PVSK/PCBM/BCP/Ag	610	21.00	68.00	8.71	[79]
PEA _x FA _{1-x} SnI ₃ (NH ₄ SCN)	ITO/PEDOT:PSS/PVSK/ICBA/BCP/Ag	940	17.40	75.00	12.40	[80]
FA _{0.9} PEA _{0.1} SnI ₃	ITO/PEDOT:PSS/PVSK/ICBA BCP/Al	651	16.88	64.00	7.05	[81]
FASnI ₃ -50%LFA	ITO/PEDOT:PSS/PVSK/C60/BCP/Ag	616	22.08	72.80	9.90	[82]
(FA _{0.9} EA _{0.1}) _{0.98} EDA _{0.01} SnI ₃ (GeI ₂)	FTO/PEDOT:PSS/PVSK/C60/BCP/Ag/Au	840	20.38	74.00	13.24	[83]
FASnI ₃ (5% PHCl)	ITO/PEDOT:PSS/FASnI ₃ /C60/BCP/Ag	760	23.50	64.00	11.40	[84]
FA _{0.8} GA _{0.2} SnI ₃ /AN ₂ FA _{n-1} Sn _n I _{3n+1}	ITO/PEDOT:PSS/PVSK/C60/BCP/Ag	645	21.10	76.30	10.40	[85]
CsSnI ₃	ITO/PEDOT:PSS/CsSnI ₃ /C60/BCP/Cu	630	19.70	66.10	8.20	[86]
FASnI ₃ Br _{3-x} (5% PhNHNH ₃ Cl)	ITO/PEDOT:PSS/PVSK/C60/BCP/Ag	760	22.95	70.98	12.38	[87]
FA _{0.9} SnI ₃ (10% FPEABr)	ITO/PEDOT:PSS/PVSK/ICBA/BCP/Al	828	24.50	69.40	14.03	[88]
FASnI ₃	FTO/(PEG)-PEDOT:PSS/PVSK/PCBM/BCP/Ag	370	22.06	62.70	5.12	[89]
TG-FASnI ₃	ITO/PEG-PEDOT:PSS/PVSK/C60+BCP/Ag	695	22.01	73.30	11.22	[90]
MASnI ₃	ITO/PEDOT:PSS/Poly-TPD/PVSK/C60/BCP/Ag	377	12.10	36.60	1.70	[91]
(PEA) ₂ (FA) _{n-1} Sn _n I _{3n+1}	ITO/LiF/PEDOT:PSS/PVSK/C60/BCP/Ag	470	20.07	74.00	6.98	[92]

To investigate the doping-effect difference between Spiro-OMeTAD + Li-TFSI + tBP and PTAA + LiTFSI + tBP, Handa et al. investigated the near-band-edge optical response devices based on FTO/c-TiO₂/mp-TiO₂/MASnI₃/HTL/Au structure and the source of voltage loss in the devices [50,51]. The methods used to prepare the hole transport layer were all toluene solution of hole transport materials with Li-TFSI (acetonitrile) solution and tBP additives. The photovoltaic parameters extracted after 20 days of preparation were as follows: 26.10 mA/cm² short circuit current density, 300 mV open-circuit voltage, 30% fill factor. The short-circuit current density of the device was slightly higher than that of its lead-based counterpart (24 mA/cm²), since MASnI₃ perovskite can absorb more photons in the near-infrared region up to 1000 nm. However, the photoconversion efficiency is about 2.30%, because the open-circuit voltage was only 230 mV and the fill factor was only 39% (Table 2). The replacement of Spiro-OMeTAD with PTAA did not fundamentally solve the issue of additive use on the tin-based perovskite films, and the HOMO energy level of PTAA (−5.10 eV) does not match the valence band energy level of MASnI₃ (−4.75 eV), induced an energy barrier for the hole carrier transport.

3.1.2. PTAA:4-Isopropyl-4'-methylidiphenyliodonium Tetrakis (Pentafluorophenyl)borate (TPFB)

In 2016, with TPFB as the hole transport layer, Ke et al. prepared tin-based perovskite photovoltaic devices with FTO/c-TiO₂/mp-TiO₂/FASnI₃/PTAA:TPFB/Au structure (Figure 7a) [52]. The TiO₂-ZnS electron transfer layer effectively facilitates electron extraction from FASnI₃ into TiO₂, resulting in devices with efficient electron transfer and lower interface recombination. The champion performing perovskite solar cell achieved a photovoltaic conversion efficiency of 5.27% with an open-circuit voltage of 380 mV, a short-circuit current density of 23.09 mA/cm², and a fill factor of 60% (Figure 7c and Table 2). Figure 7d shows that the perovskite solar cell exhibits good reproducibility and high average performance cells. The hole transport material consists of 32 mg PTAA and 3.6 mg TPFB in 1.6 mL chlorobenzene solution. Among them, the valence band maximum of FASnI₃ (−4.7 eV) is slightly higher than that of PTAA (−5.2 eV), which may present a

barrier to hole carrier transport (Figure 7b). However, the FASnI₃ film is briefly exposed to air during device fabrication, so the surface of the perovskite film is p-type doped and forms an ohmic contact with the PTAA layer. Therefore, the hole carriers can be efficiently transferred from perovskite FASnI₃ to hole transport PTAA layer.

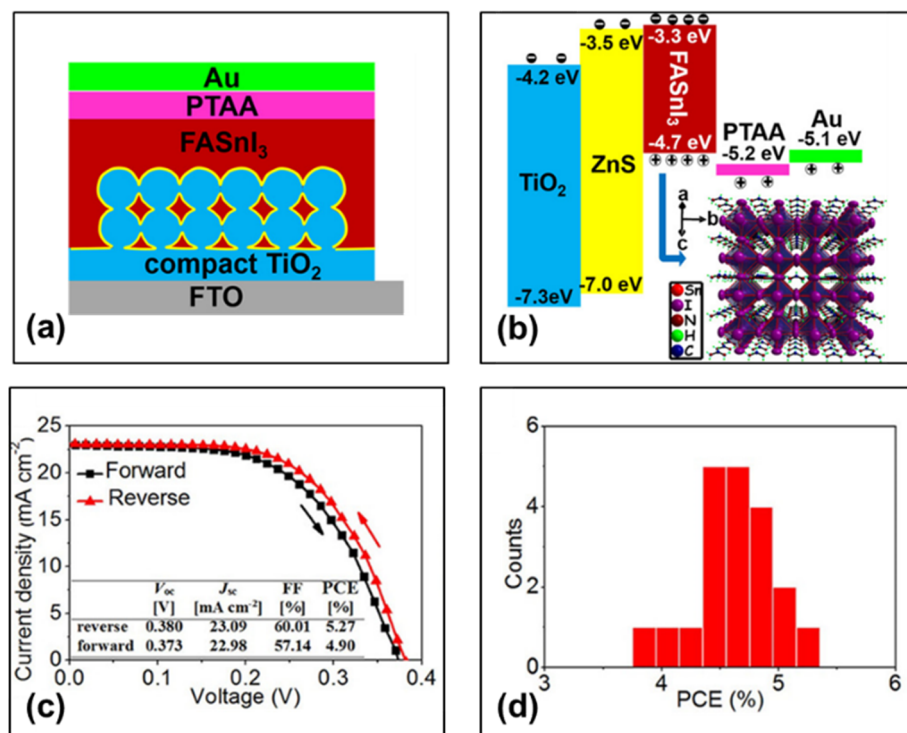


Figure 7. (a) Schematic diagram of the device structure and (b) energy band diagram of the FASnI₃ solar cell and crystal structure of the perovskite light absorber. (c) Current density–voltage curves of the champion performing FASnI₃ solar cell using mesoporous TiO₂-ZnS measured at reverse and forward voltage scans. (d) PCE histograms of 20 FASnI₃ solar cells using mesoporous TiO₂-ZnS measured under reverse voltage scan [52]. Reprinted with permission from Ref. [50]. Copyright 2016 American Chemical Society.

Subsequent research groups have conducted several investigations on tin-based perovskite solar cells based on the hole transport layer of PTAA:TPFB [47,53–58]. Among them, Yang et al. used PTAA+TPFB as the hole transport layer, en-FASnI₃ as the light-absorbing layer, SnO₂-C₆₀ pyrrolidine tris-acid (CPTA) as the electron transport layer, and en-FASnI₃ to fabricate the tin-based perovskite solar cells FTO/SnO₂-CPTA/en-FASnI₃/PTAA:TPFB/Au (Figure 8a,b) [58]. Similar to the FASnI₃ perovskite layer, the valence band maximum of en-FASnI₃ was also higher than HOMO of PTAA; however, the surface of en-FASnI₃ perovskite film was p-doped, producing the ohmic contact between them. The champion device achieved a photovoltaic conversion efficiency of 7.40%, an open-circuit voltage of 720 mV, a short-circuit current density of 16.45 mA/cm², and a fill factor of 65% (Figure 8c). Meanwhile, the reproducibility of the devices was excellent, with most of them having an efficiency of more than 6% (Figure 8d).

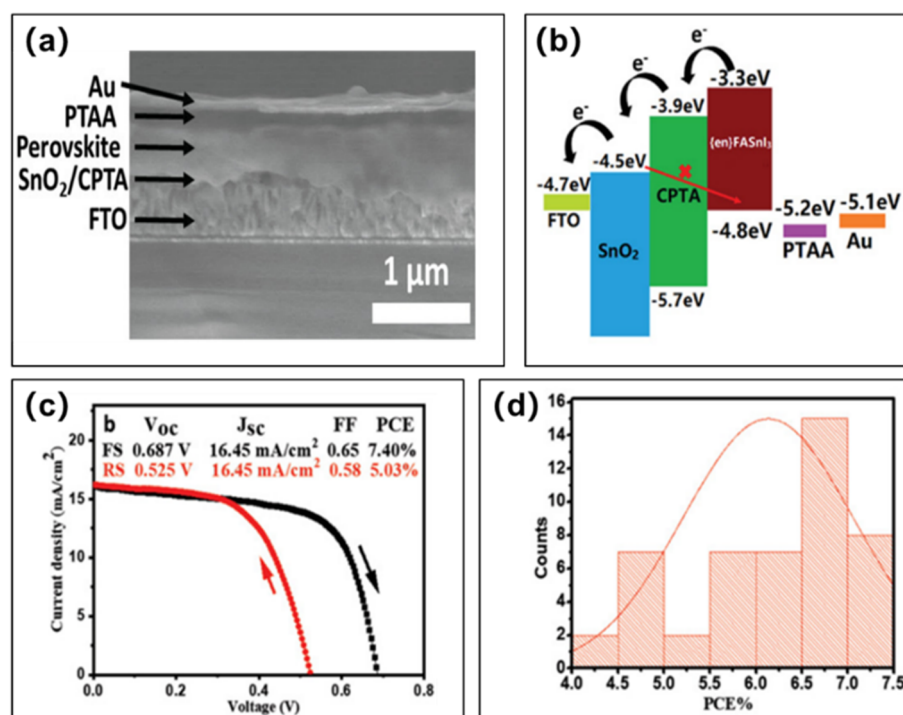


Figure 8. (a) Cross-sectional SEM image of the tin-based perovskite solar cell. (b) Energy band diagram of the tin-based perovskite solar cell. The red arrows illustrate the complex of the SnO_2 /en- FASnI_3 interface. (c) Current density–voltage curves of the champion device; the open-circuit voltages for forward and reverse scans were 687 mV and 525 mV (50 mV/s scan rate), respectively. (d) Photovoltaic conversion efficiency histograms for 48 solar cells [58]. Reprinted with permission from Ref. [56]. Copyright 2019 John Wiley and Sons.

In summary, the combination of the PTAA and TPFB as hole transport material showed great potential in the inverted FASnI_3 -based solar cells, in which the perovskite layer is exposed to air during the preparation of FASnI_3 to form surface p-type doping, so they form an ohmic contact with PTAA layer, which effectively minimized the charge carrier transport caused by the energy-level mismatch between the hole transport layer and the tin-based perovskite layer problem. Compared with Spiro-OMeTAD, Spiro-OMeTAD still failed to achieve good performance despite the use of different kinds of additives. In contrast, the PTAA cavity transport layer uses the additive TPFB, and the en- FASnI_3 -based device achieved a high performance.

3.2. Organic P3HT

Jung et al. utilized SnBr_2 and MABr for co-evaporation of lead-free MASnBr_3 perovskite crystal films (Figure 9a), and utilized three hole-transport materials Spiro-OMeTAD, C_{60} and P3HT as the hole transport layer. They finally fabricated the tin-based perovskite solar cells $\text{FTO}/\text{c-TiO}_2/\text{MASnBr}_3/\text{HTM}/\text{Au}$ [45]. The band gaps and energy levels of MASnBr_3 perovskite and the hole transport materials were measured based on the results of ultraviolet photoelectron emission spectroscopy and ultraviolet–visible absorption spectroscopy (Figure 9b). The devices prepared with Spiro-OMeTAD showed a power conversion efficiency of 0.002%, a short-circuit current density of $0.03 \text{ mA}/\text{cm}^2$, an open-circuit voltage of 236 mV, and a fill factor of 25.6%. The power conversion efficiency of the device with C_{60} was 0.22%, the short-circuit current density was $1.04 \text{ mA}/\text{cm}^2$, the open-circuit voltage was 509 mV, and the fill factor was 80%. The devices prepared with P3HT showed a power conversion efficiency of 0.35%, a short-circuit current density of $2.05 \text{ mA}/\text{cm}^2$, an open-circuit voltage of 415 mV, and a fill factor of 41%. The highest power conversion efficiency and short-circuit current density were observed in the devices with P3HT as hole transport layer (Figure 9c). Part of the current is provided by the additional

photogenerated charge of P3HT. On the other hand, a higher efficiency of up to 1.12% was obtained using P3HT as HTL when we used sequential deposition, corresponding to an open-circuit voltage of 498 mV and a short-circuit current density of 4.27 mA/cm^2 , with a fill factor of 49.10% (Table 2). Due to the low valance band level of MASnBr_3 perovskite, C60 (-6.2 eV) becomes the optimal candidate as hole transport layer among them. In addition, as expected, the open-circuit voltage of C60-based device was higher than that of P3HT (-5.1 eV)-based devices.

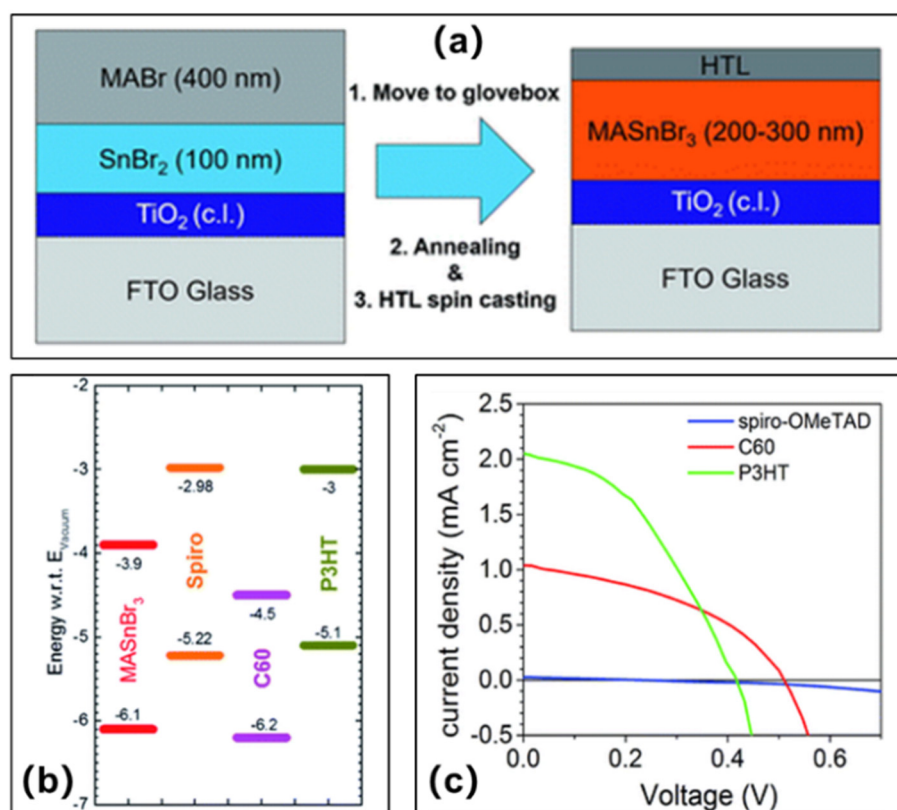


Figure 9. (a) Schematic diagram of tin-based perovskite solar cell device preparation process; the first layer is 100 nm SnBr₂, and the second layer is 400 nm MABr to avoid any air contact with elemental Sn. (b) Energy level diagram of MASnBr_3 perovskite and hole transport materials. (c) Current density–voltage curves of MASnBr_3 perovskite solar cells fabricated by co-evaporation of SnBr₂ and MABr and with Spiro-OMeTAD (blue), C₆₀ (red) and P3HT (green) [45]. Reprinted with permission from Ref. [44]. Copyright 2016 The Royal Society of Chemistry.

In 2016, with P3HT as hole transport materials, Qiu et al. prepared mesoporous solar cells with FTO/c-ZnO/n-ZnO/Cs₂SnI₆/P3HT/Ag structures using air-stable perovskite Cs₂SnI₆ as the light-absorbing material (Figure 10a,b) [59]. In this case, the P3HT precursor solution was prepared by dissolving 10 mg of P3HT in 1 mg of chlorobenzene; and the devices with ZnO nanorods grown in the PLD-ZnO seed layer showed improved performance than those with spin-coated seed layer (Figure 10d), finally obtaining a power conversion efficiency of nearly 1%, a short-circuit current density of 3.20 mA/cm^2 , an open-circuit voltage of 520 mV and a fill factor of 51.50% (Figure 10c,d, Table 2). The energy-level alignments of conduction and valance bands of the Cs₂SnI₆ perovskite allow for the efficient injection of electrons into the electron transport layer and transport of holes to the P3HT layer.

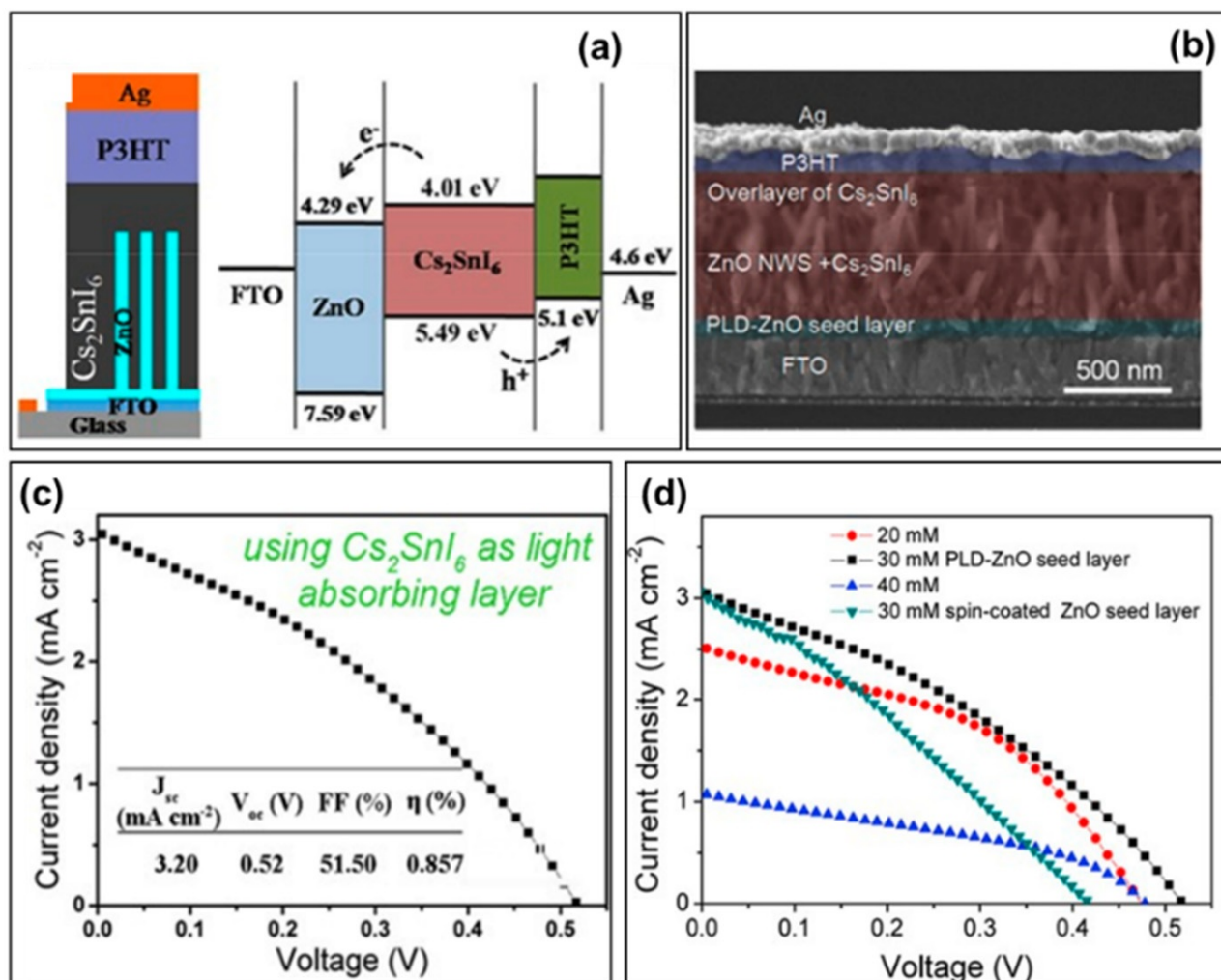


Figure 10. (a) Device and energy band structure of FTO/ZnO dense layer/ZnO nanorods/ Cs_2SnI_6 /P3HT/Ag solar cell. (b) Cross-sectional SEM images of the device structure. (c) Current density–voltage curves of the solar cell based on Cs_2SnI_6 . (d) J–V curves of Cs_2SnI_6 perovskite solar cells with ZnO nanorods grown on different seed layers and different precursors [59]. Reprinted with permission from Ref. [57]. Copyright 2016 John Wiley and Sons.

In 2017, Qiu et al. utilized B- γ - CsSnI_3 that spontaneously oxidizes to air-stable Cs_2SnI_6 and prepared FTO/ TiO_2 / Cs_2SnI_6 /P3HT/Ag-structured perovskite solar cells (Figure 11a,b) [60]. By optimizing the thickness of the perovskite absorber layer, a power conversion efficiency of about 1% was achieved at an open-circuit voltage of 510 mV and a short-circuit current of 5.41 mA/cm^2 (Figure 11c, Table 2). For the devices with all-inorganic perovskite material Cs_2SnI_6 as the light-absorbing layer, among the hole transport layers of Spiro-OMeTAD, C_{60} and P3HT, the devices with P3HT as the hole transport layer exhibited the highest power conversion efficiency and short-circuit current density. This can be explained by the HOMO of P3HT (−5.10 eV) matching well with the valence band of the all-inorganic perovskite material Cs_2SnI_6 (−5.49 eV). The device performance decreased thereafter and failed after about one month. The organic hole transport material P3HT was considered as one of most problematic sources responsible for the performance loss.

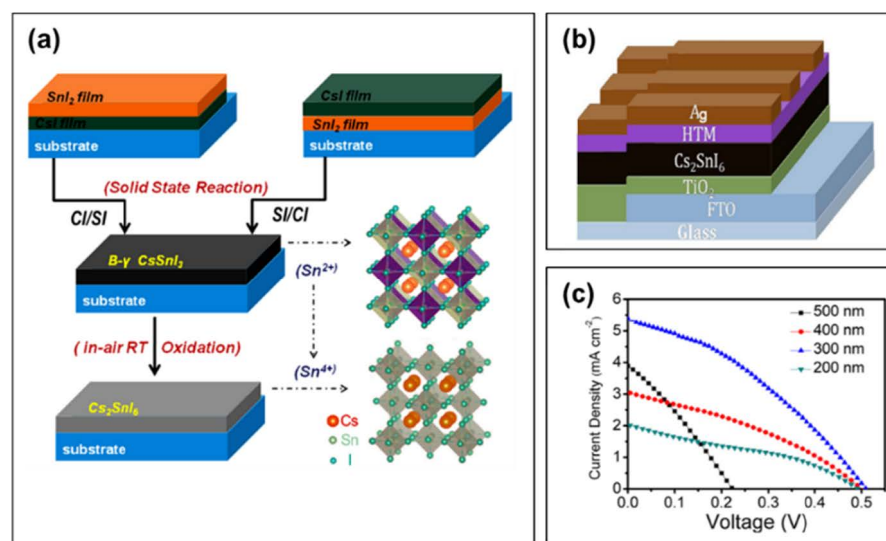


Figure 11. (a) Schematic diagram of the growth of Cs₂SnI₆ film from CsSnI₃ by a two-step deposition method; the perovskite crystal structures of Cs₂SnI₆ and CsSnI₃ at the bottom right of the figure. (b) Schematic diagram of the structure of Cs₂SnI₆-based perovskite solar cells. (c) Current density–voltage curves of perovskite solar cells fabricated based on Cs₂SnI₆ with different thicknesses [60]. Reprinted with permission from Ref. [58]. Copyright 2017 Elsevier.

3.3. Organic Small Molecule TPE

In 2018, Ke et al. synthesized a novel small molecule hole transport layer material tetraphenylamine (TPE), which is a compound with excellent physicochemical properties, such as easy dissolution in common organic solvents to form uniform films [41]. The mobility was comparable to that of doped Spiro-OMeTAD and PTAA: $1.4 \pm 0.1 \times 10^{-3}$, $1.3 \pm 0.1 \times 10^{-3}$, and $1.6 \pm 0.2 \times 10^{-3} \text{ cm}^2 \text{V}^{-1} \text{s}^{-1}$, respectively. The HOMO energy level was -4.99 eV and LUMO energy level was -2.22 eV , which match well with the tin-based perovskite energy level. In addition, the TPE exhibited good thermal stability with high decomposition temperature of 425°C . The tin-based perovskite solar cell with FTO/c-TiO₂/mp-TiO₂/en-FASnI₃/TPE/Au was prepared (Figure 12a). TPE precursor solution was prepared by adding 5 mg of TPE in a mixture of 0.5 mL of chlorobenzene and 0.5 mL of chloroform. As shown in Figure 12c, the TPE-coated perovskite film showed a good quenching effect, implying that the photogenerated carriers were more efficiently transported into the TPE carrier transport layer. As a result, the good hole transport ability of TPE allowed the solar cell to have a high short-circuit current density and fill factor and the champion stability (Figure 12d). Finally, the solar cell exhibited a power conversion efficiency of 6.85%, an open-circuit voltage of 453 mV, a short-circuit current density of 22.60 mA/cm^2 , and a fill factor of 67% measured under the forward voltage scan. Under the reverse scan, the power conversion efficiency was 7.23%, the open-circuit voltage was 459 mV, the short-circuit current density was 22.54 mA/cm^2 , and the fill factor was 70%. Moreover, the hysteresis was quite small (Figure 12b). Since TPE had several advantages such as low cost, easy preparation, well-matched tin-based perovskite energy levels, high mobility and excellent thermal stability, etc., it is well suited to be used as a superior hole transport material for the development of economical and high-performance tin-based perovskite solar cells. The devices using the TPE as the hole transport layer had achieved improved performance compared to that of Spiro-OMeTAD- and PTAA-doped devices, even without adding any additives or dopants in TPE, which showed great potential for the fabrication of low-cost, high-efficiency and large-scale tin-based perovskite solar cells (Figure 13).

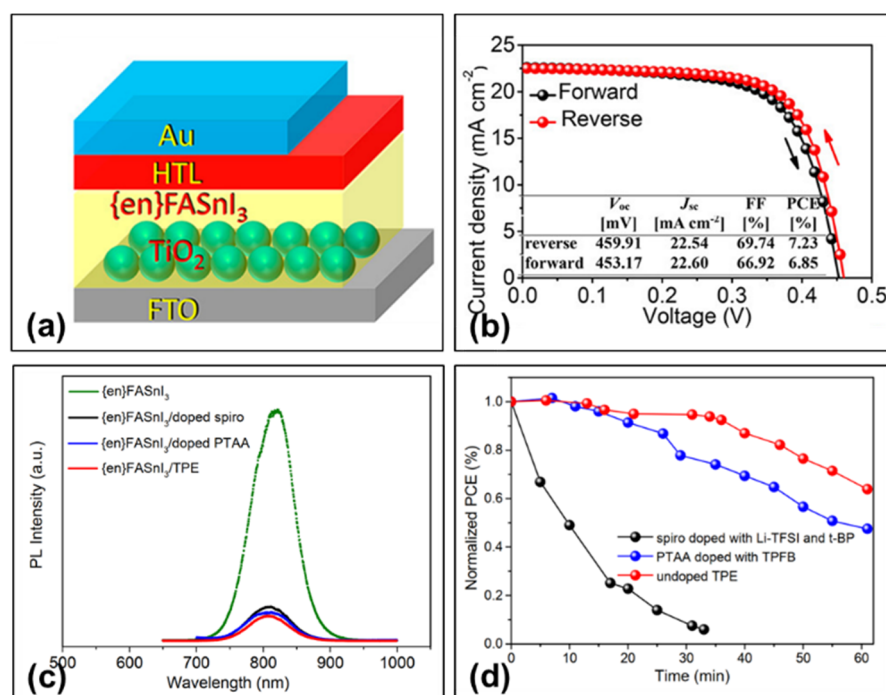


Figure 12. (a) Device structure of TPE-based perovskite solar cell. (b) Current density–voltage curves of the champion perovskite solar cell under reverse and forward voltage scans. (c) Photoluminescence spectra of perovskite films with different hole transport layers. (d) Aging tests of unencapsulated solar cells with various hole transport layers in ambient air [41]. Reprinted with permission from Ref. [40]. Copyright 2018 American Chemical Society.

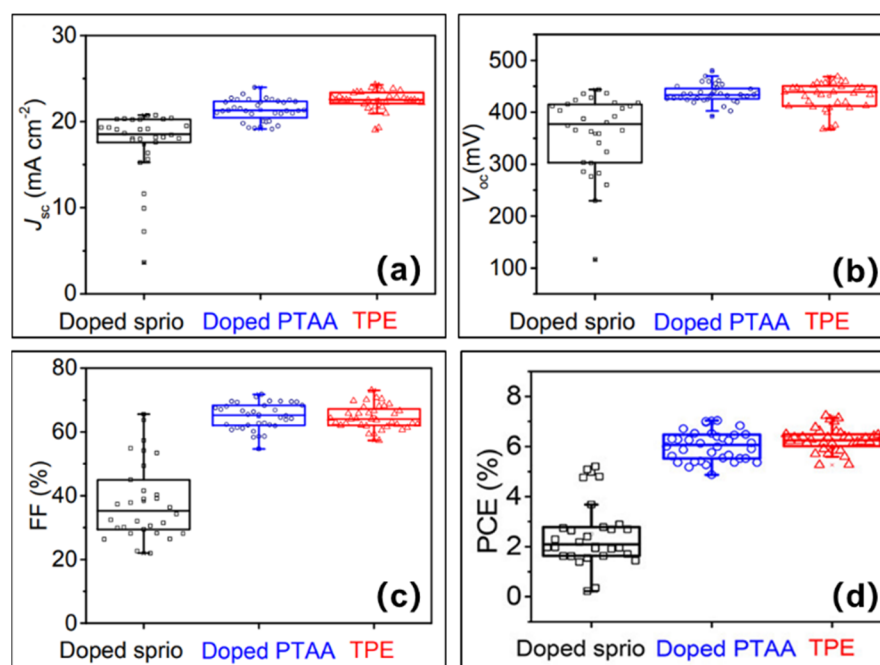


Figure 13. Statistics of (a) short-circuit current, (b) open-circuit voltage, (c) fill factor and (d) power conversion efficiency for FASnI₃-based solar cells with different hole transport layers [41]. Reprinted with permission from Ref. [40]. Copyright 2018 American Chemical Society.

In summary, regarding the use of PTAA + Li-TFSI + tBP, there are easily caused issues that arise from the incorporation of dopants. This is not to say that all dopants will destroy

the perovskite film, with TPFB used as the dopant in PTAA layer, it still obtains a good performance. The FASnI₃-based perovskite solar cells eventually achieved a 7.40% power conversion efficiency and 720 mV open-circuit voltage. For undoped P3HT, in Cs₂SnI₆-based perovskite solar cells, the power conversion efficiency and short-circuit current density in P3HT-based devices were higher than those in Spiro-OMeTAD and C₆₀-based devices. In addition, for the undoped TPE, in FASnI₃-based perovskite solar cells, the short-circuit current density and open-circuit voltage were higher than those in doped Spiro-OMeTAD and C₆₀-based device. However, Spiro-OMeTAD and doped PTAA-based devices showed small hysteresis and quite good reproducibility. In general, the HOMO level of the perovskite layer matches well with that of the hole transport layer. The HOMO level of tin-based perovskite is slightly deeper than that of hole transport materials, which is favorable for charge carrier transport. For example, the HOMO energy level of P3HT is −5.10 eV, which matches well with that of Cs₂SnI₆ energy level (−5.49 eV); TPE (−4.99 eV) and en-FASnI₃ (−4.80 eV), which also matched well. TPE has a shallower energy level than that of Spiro-OMeTAD and PTAA, which means they have a lower energy mismatch; thus, a higher short-circuit current density and open-circuit voltage can be achieved.

3.4. Commonly Used Hole Transfer Material Poly(3,4-thylenedioxythiophene): Polystyrene Sulfonate (PEDOT:PSS)

Although the performance of tin-based perovskite photovoltaic devices with regular device structure has been improved in the past few years, from the perspective of the device preparation process: (i) The quality of tin-based perovskite films deposited on electron transport layers (e.g., TiO₂, C₆₀, ZnO, and ZrO) is poor, which leads to poor interfacial contacts and instability issues in photovoltaic devices. (ii) The use of additives in hole transport layer on the tin-based perovskite layer would damages the perovskite film. Thus, obtaining high-performance devices with a regular structure is still challenging. While inverted tin-based solar cell devices can avoid these problems to some extent.

In inverted structured tin-based perovskite solar cells, PEDOT:PSS is the most commonly used hole transport layer material [61–88,93,94]. In 2016, Liao et al. used PEDOT:PSS as the hole transport layer and synthesized high-quality, uniform, full-coverage FASnI₃ perovskite films using SnF₂ as additive. The SnF₂ additive inhibits the oxidation of Sn²⁺ in tin-based perovskites and reduces the hole density in the synthesized films [61]. Moreover, the spin-coating of diethyl ether on PEDOT:PSS/ITO substrate produces a more uniform and complete coverage of the perovskite films. Finally, they prepared inverted devices with the structure of ITO/PEDOT:PSS/FASnI₃ + 10 mol% SnF₂/C₆₀/BCP/Ag (Figure 14a,b). The device achieved a power conversion efficiency of 6.22%, an open-circuit voltage of 465 mV, a short-circuit current density of 22.07 mA/cm² and a fill factor of 60%. Meanwhile, the device exhibited a negligible current density–voltage hysteresis behavior under the forward and reverse scan (Figure 14c, Table 2). Among the 30 devices fabricated in the same batch, the average power conversion efficiency was $5.41 \pm 0.46\%$, the average open-circuit voltage was 449 ± 23 mV, the average short-circuit current density was 20.69 ± 0.95 mA/cm², and the average fill factor was $58.20 \pm 2.50\%$ (Figure 14d) with good reproducibility. After the reports of Snaith et al. and Kanatzidis et al. in 2014 [25,26], Liao's work was considered as another substantial improvement in the power conversion efficiency of tin-based perovskite solar cells. The PEDOT:PSS was used as the anode buffer layer and the hole transport layer to transport holes from the perovskite to the ITO anode, but the HOMO energy level of the PEDOT:PSS is slightly higher in the energy diagram shown in Figure 14b. The light-intensity-dependence measurement suggested that the open-circuit voltage was limited by the imbalanced charge carrier transport at the HTL/FASnI₃ and FASnI₃/ETL interface, which was not ideal for optimal device performance, and more work was needed in hole transport layer optimization and interface engineering, to further improve the performance of Sn-based perovskite solar cells.

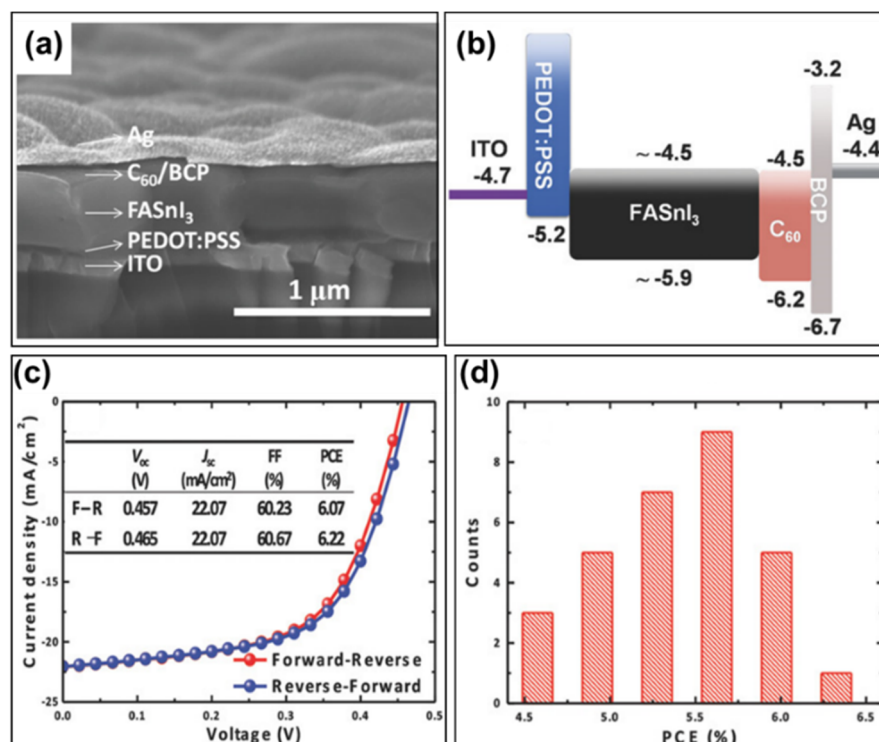


Figure 14. FASnI₃-based inverted perovskite solar cell: (a) Cross-sectional SEM image of the device. (b) Schematic diagram of the energy levels. (c) Current density–voltage curve characteristics at AM1.5G illumination under reverse and forward scans. (d) Power conversion efficiency histograms of 30 solar cell devices with 10% SnF₂ additive [61]. Reprinted with permission from Ref. [59]. Copyright 2016 John Wiley and Sons.

Subsequently, with PEDOT:PSS as the hole transport layer and with mixed FA and MA cations (FA)_x(MA)_{1-x}SnI₃ perovskite material as the light absorber layer, Zhao et al. fabricated solar cell devices with the structure of ITO/PEDOT:PSS/(FA)_x(MA)_{1-x}SnI₃/C₆₀/BCP/Ag (Figure 15a) [64]. The final device achieved a maximum power conversion efficiency of 8.12% (7.74%, reverse scan), corresponding to a short-circuit current density of 21.2 (21.0, reverse scan) mA/cm², an open-circuit voltage of 610 (610, reverse scan) mV, a fill factor of 62.70% (60.40%, reverse scan), and a negligible hysteresis (Figure 15c and Table 2). The surface of PEDOT:PSS is treated by organic ammonium salts in the perovskite, thus reducing the work function of PEDOT:PSS (−5.0 eV) during perovskite deposition, which was around −4.7 eV. In other words, the treatment mitigated the mismatch between the valence band of tin-based perovskite (−4.80 eV) and HOMO of PEDOT:PSS, since the work function was more or less lowered during the perovskite deposition (Figure 15b). In the forward scan mode, the average power conversion efficiency of the 30 devices was 7.29 ± 0.55%, the average open-circuit voltage was 570 ± 20 mV, the average short-circuit current density was 20.70 ± 0.60 mA/cm², and the average fill factor was 61.60 ± 2.50%, which showed a high reproducibility during the device fabrication (Figure 15d).

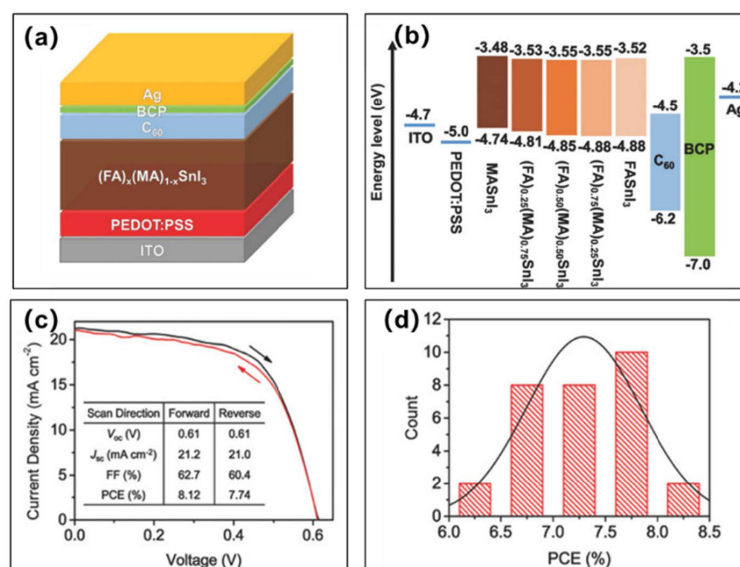


Figure 15. (a) Schematic diagram of the device structure. (b) Device energy level diagram. (c) Current density–voltage curves of the champion devices measured in forward and reverse scan. (d) Power conversion efficiency histograms from multiple batches [64]. Reprinted with permission from Ref. [62]. Copyright 2017 John Wiley and Sons.

In 2021, with PEDOT:PSS as the hole transport layer, and with 2D/3D structure phenethylammonium bromide (FPEABr)/FASnI₃ as the perovskite light-absorption layer, Yu et al. fabricated the device ITO/PEDOT:PSS/Perovskite/ICBA/BCP/Al. The unique 2D/3D structure effectively suppressed the oxidation of Sn²⁺ to Sn⁴⁺ and reduced the defect density. Moreover, the 2D layer at the perovskite/PEDOT:PSS interface inhibits the migration of iodine ions from tin perovskite to the hole transport material PEDOT:PSS layer [88]. Finally, the device achieved a certified efficiency of 14.03%, corresponding to an open-circuit voltage of 828 mV, a short-circuit current of 24.50 mA/cm², and a fill factor of 69.40% (Table 2). The 2D/3D tin-based perovskite films have a shallower valence band value (−5.05 eV) than that of FASnI₃ (−5.15 eV) film, which matches better with the adjacent PEDOT:PSS layer (−5.0 eV). This will enhance the charge carrier extraction at the perovskite/PEDOT:PSS interface and improve the device performance. In addition to these groups mentioned above, there are several other research groups who have employed PEDOT:PSS as the hole transport material and also achieved excellent performance. The device-efficiency records of their work are shown in Figure 16.

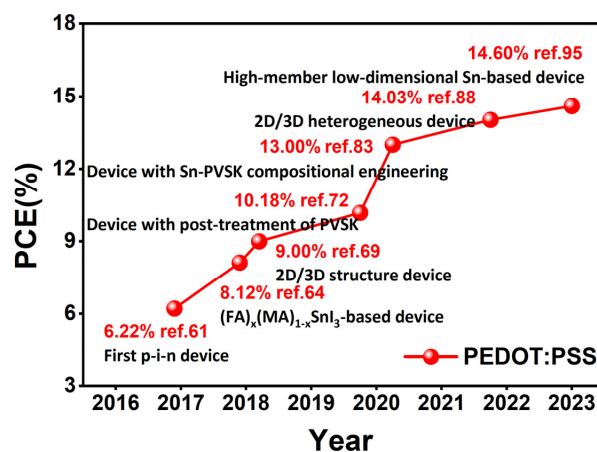


Figure 16. Efficiency development diagram of tin-based perovskite solar cells with pure PEDOT:PSS as hole transport layer [61,64,69,72,83,88,95].

Typically, the work function of PEDOT:PSS is -5.20 eV; however, the work function of PEDOT:PSS can be modified. When the surface of PEDOT:PSS is treated by the organic ammonium salt $\text{FA}_{0.75}\text{MA}_{0.25}\text{SnI}_3$ (-4.80 eV), the work function of PEDOT:PSS was modified to -5.0 eV, which reduces the energy-level mismatch between them. The HOMO energy level of the PEDOT:PSS layer should be higher than that of the perovskite layer, but the energy gap between them should not too high; for example, the HOMO gap between PEDOT:PSS (-5.20 eV) and FASnI_3 (-5.90 eV) is too high, which is not ideal for device performance.

3.4.1. Polyethylene Glycol (PEG)-PEDOT:PSS

The current density–voltage hysteresis in perovskite solar cells presents a serious issue because it affects the power conversion efficiency and stability of the devices. In a previously conducted experiment, 0.05%, 0.1% and 0.2% (volume ratio) PEG-400 were added to an aqueous solution of PEDOT:PSS, and the devices with the structure of FTO/(PEG-)PEDOT:PSS/ FASnI_3 /PCBM/BCP/Ag were prepared (Figure 17a) [89]. The devices based on 0.2% PEG-PEDOT:PSS showed the champion performance with power conversion efficiencies of 5.12% and 5.03%; open-circuit voltages of 370 mV and 360 mV, short-circuit current densities of 22.06 mA/cm^2 and 21.90 mA/cm^2 , and the fill factor of 62.70% and 63.80% in the forward and reverse scan, respectively (Table 2). A significant reduction in hysteresis was also shown, in addition to high reproducibility and an improved device stability with 4.91% stable efficiency (Figure 17c,d and Figure 18). The concentration of PEG could modulate the work function of this hole transport layer, thus reducing the energy-level mismatch between the hole transport layer and the tin-based perovskite layer; the valence band of FASnI_3 is -4.74 eV and the work function of PEDOT:PSS is -5.10 eV, with an energy level mismatch of about 0.36 eV between them. After 0.2% PEG-doping in PEDOT:PSS, the energy-level mismatch between FASnI_3 and PEG-PEDOT:PSS was decreased to 0.05 eV (Figure 17b).

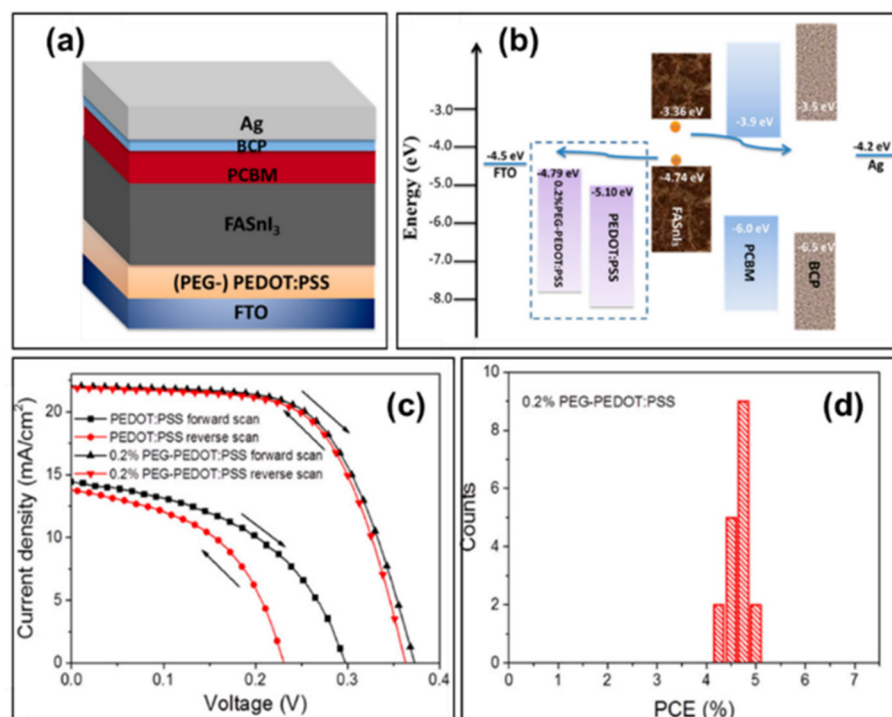


Figure 17. (a) Schematic diagram of the device structure. (b) Device energy level diagram. (c) Current density–voltage curves of devices with PEDOT:PSS and 0.2% PEG-PEDOT:PSS as the hole transport layer. (d) Power conversion efficiency histogram of 18 FASnI_3 devices based on 0.2% PEG-PEDOT:PSS [89]. Reprinted with permission from Ref. [90]. Copyright 2018 American Chemical Society.

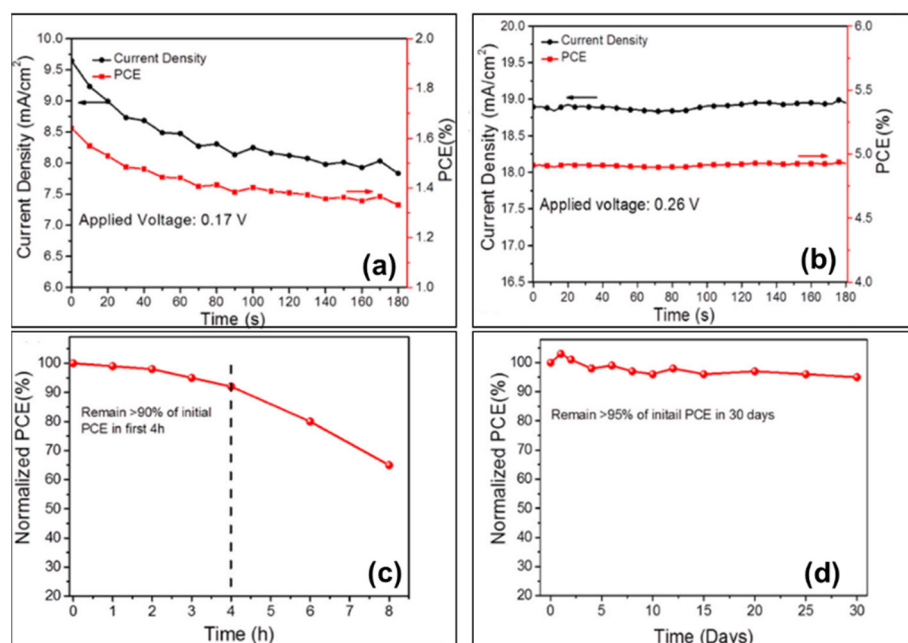


Figure 18. Steady-state current density and stable power conversion efficiency of devices based on (a) PEDOT:PSS and (b) 0.2% PEG-PEDOT:PSS under continuous AM 1.5G illumination, devices based on 0.2% PEG-PEDOT:PSS were tested for device stability during storage (c) under ambient conditions and (d) in a glove box filled with N₂ [89]. Reprinted with permission from Ref. [90]. Copyright 2018 American Chemical Society.

Moreover, with PEG-PEDOT:PSS as the hole transport layer, in 2020, Liu et al. prepared thin-based perovskite solar cells with the structure ITO/PEG-PEDOT:PSS/TG-FASnI₃/C₆₀/BCP/Ag [90]. The highly crystalline TG-FASnI₃ films were prepared by pre-treating FASnI₃ perovskite films with organic halide salt n-propylammonium iodide (PAI) solution prior to annealing. The device achieved a certified stable efficiency of 11.22%, corresponding to an open-circuit voltage of 695 mV, a short-circuit current of 22.01 mA/cm², and a fill factor of 73.30% (Table 2). Under 1000 h AM 1.5G illumination, the TG-FASnI₃ cell encapsulated in the N₂ glove box still maintains more than 95% of its initial efficiency. The use of PEG makes the work function of the hole transport layer adjustable, which can effectively reduce the energy-level mismatch between FASnI₃ and PEDOT:PSS without damaging the stability of the device, and endows the device with high repeatability and negligible hysteresis, which effectively improves the device performance.

3.4.2. PEDOT:PSS/Poly-TPD

Typically, poly[*N,N'*-bis(4-butylphenyl)-*N,N'*-bis(phenyl)benzidine] (Poly-TPD) was used as the hole transport layer as well as the electron blocking layer proposed in [96], Yu et al. used PEDOT:PSS/Poly-TPD as the hole transport layer and prepared the device ITO/PEDOT:PSS/Poly-TPD/MASnI₃/C₆₀/BCP/Ag (Figure 19a) [91]. The PEDOT:PSS layer was deposited by spin-coating from aqueous solution and the Poly-TPD layer was deposited by spin-coating from 10 mg/mL of chlorobenzene solution. The final solar cell achieved a power conversion efficiency of 1.7%, with an open-circuit voltage of 377 mV, a short-circuit current density of 12.1 mA/cm², and a fill factor of 36.6% (Table 2). The HOMO of MASnI₃ is −5.47 eV, and the energy level gap between PEDOT:PSS/MASnI₃ was 0.27 eV; the HOMO of Poly-TPD was −5.40 eV, thus the energy level gap between Poly-TPD/MASnI₃ was only 0.07 eV (Figure 19b). By combining the Poly-TPD layer with the PEDOT:PSS layer, the external quantum efficiency values were enhanced over the entire wavelength range, indicating that the charge carrier recombination was reduced with the introduction of the Poly-TPD layer (Figure 19c). The perovskite solar cell with PEDOT:PSS/Poly-TPD hole transport bilayer showed a higher short-circuit current density

(5.1 mA/cm²) and a higher open-circuit voltage (494 mV) than that of devices with only PEDOT:PSS layer (a short-circuit current density of 3.5 mA/cm² and an open-circuit voltage of 470 mV) (Figure 19d). In general, the introduction of Poly-TPD enlarges the grain size of perovskite film deposited on it more than that of perovskite film deposited on PEDOT:PSS, which is conducive to more efficient charge extraction. Moreover, the use of Poly-TPD layer reduces charge recombination and improves the energy level matching effect with perovskite layer. Finally, the open-circuit voltage and short-circuit current of the device are improved.

3.4.3. LiF/PEDOT:PSS

Ran et al. inserted LiF between the ITO and PEDOT:PSS layer to promote fast hole extraction, and with (PEA)₂(FA)_{n-1}Sn_nI_{3n+1} as the perovskite light-absorption layer. They prepared 2D/3D tin-based perovskite solar cells ITO/LiF/PEDOT:PSS/perovskite/C₆₀/BCP/Ag (Figure 20b) [92]. The device showed a maximum photoelectric conversion efficiency of 6.98%, a short-circuit current density of 20.07 mA/cm², an open-circuit voltage of 470 mV, and a fill factor of 74% (Figure 20a,b and Table 2). After inserting LiF between ITO and PEDOT:PSS, the tunnelling effect of the ultrathin LiF insulating layer itself can reduce the energy barrier at the ITO/PEDOT:PSS interface, and the higher wettability of the LiF layer can improve the morphology of PEDOT:PSS layer, so the holes collected in PEDOT:PSS can be rapidly extracted by LiF through ITO for carrier extraction, which in turn effectively suppresses carrier recombination at the PEDOT:PSS/ITO interface. A high short-circuit current density and fill factor could be achieved based on this device. On the other hand, due to the different wettability of different thicknesses of LiF layers, it will change the molecular orientation of the PEDOT:PSS films, which finally adjusts the work function and makes the energy level well matched between the hole transport layer and the perovskite light absorber layer. The well-matched energy level not only reduced the charge carrier recombination between the ITO/PEDOT:PSS interface, it also increased the hole extraction, which further improved the open-circuit voltage and fill factor of the device (Figure 20c,d) [97–101]. The LiF insulating layer could (i) lower the work function of PEDOT:PSS, (ii) reduce the energy barrier at the ITO/PEDOT:PSS interface and (iii) reduce the charge recombination at the interface. Due to the improved hole extraction at the ITO/PEDOT:PSS interface, this bifunctional LiF layer further improves the open-circuit voltage and filling factor of the perovskite devices.

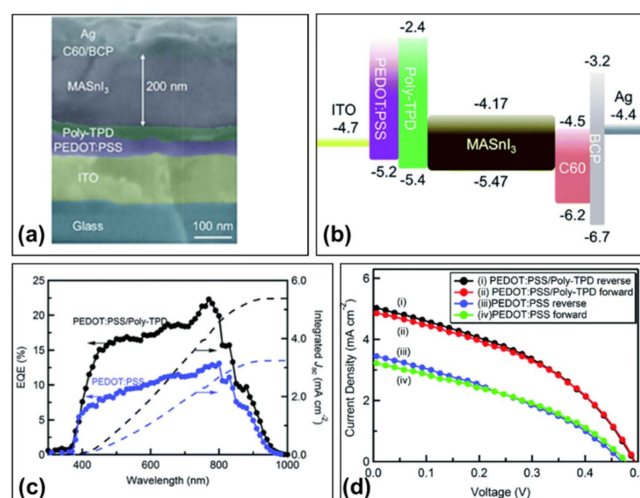


Figure 19. (a) Cross-sectional SEM image of the PEDOT:PSS/Poly-TPD-based perovskite solar cell. (b) Schematic diagram of the energy band of the device. (c) External quantum efficiency and (d) Current density–voltage curves of MASnI₃ perovskite cells using PEDOT:PSS and PEDOT:PSS/Poly-TPD as electron selective layers [91]. Reprinted with permission from Ref. [93]. Copyright 2016 The Royal Society of Chemistry.

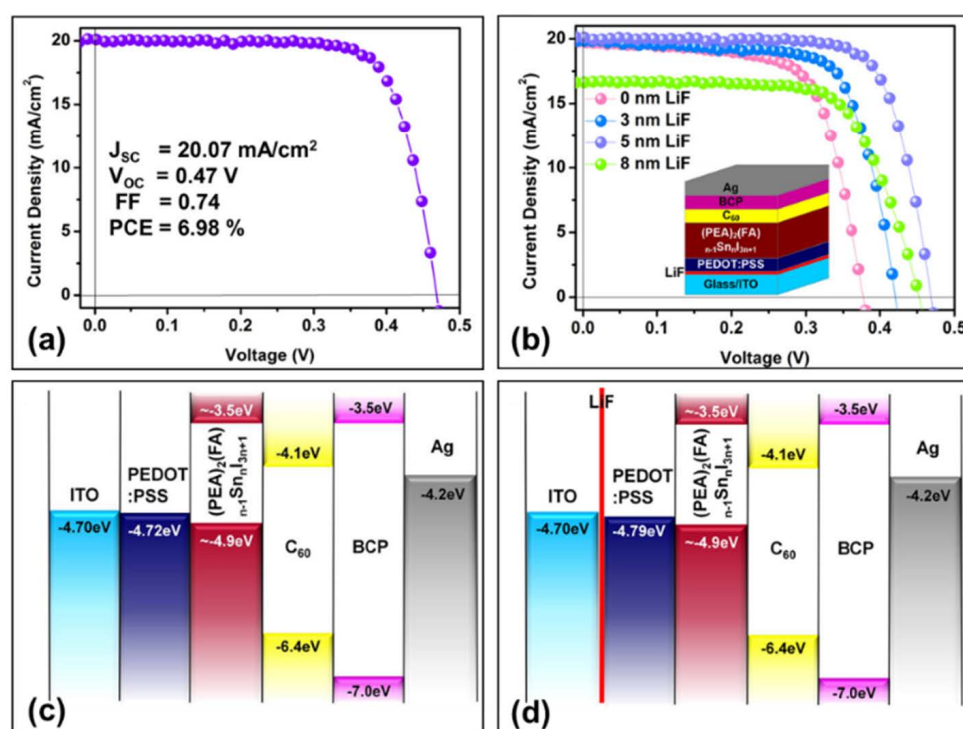


Figure 20. (a) The current density–voltage curve of the champion device. (b) Current density–voltage curves for devices with different LiF layer thicknesses; the inset shows the device structure of the perovskite solar cell. Energy band alignment diagrams for devices (c) without and (d) with ultra-thin LiF layers [92]. Reprinted with permission from Ref. [94]. Copyright 2018 American Chemical Society.

The above three methods all optimize the energy level match between hole transport layer and perovskite layer: with the addition of PEG in PEDOT:PSS, the energy level difference between 0.2% PEG-PEDOT:PSS (−4.79 eV) and FASnI₃ (−4.74 eV) is only 0.05 eV. While the other two methods both add a thin layer on top of the PEDOT:PSS layer, the Poly-TPD energy level (−5.40 eV) matches better with MASnI₃ (−5.47 eV), and the LiF layer changes the PEDOT:PSS function from −4.72 eV to −4.79 eV, which matches well with the tin-based perovskite layer (−4.90 eV). Furthermore, the addition of a functional layer has the effect of optimizing the device performance, for example, the Poly-TPD layer can play the role of blocking electrons and reducing the charge carrier recombination; the ultra-thin LiF layer can allow the holes to be easily collected in PEDOT:PSS and rapidly extracted to ITO based on its tunnelling effect.

4. Inorganic Materials

The hole transport materials used for perovskite solar cells are usually divided into organic and inorganic materials. Organic materials mainly include Spiro-OMeTAD, PTAA, PEDOT:PSS and TPE as mentioned above. Scientists have also replaced organic materials with inorganic materials, which exhibit better stability and higher carrier transport mobility, such as NiOx, CuSCN, etc. These materials have also been used to prepare inverted structure of perovskite solar cell devices.

4.1. Inorganic NiOx

With NiOx as the hole transport layer and B-γ-CsSnI₃ as the perovskite light absorption layer, Wang et al. and Zhou et al. prepared photovoltaic devices with the structure ITO/NiOx/CsSnI₃/PCBM/Al (Figure 21a) [40]. NiOx dense films were prepared by magnetron sputtering process to deposit 10 nm NiOx films and then spin-coated nickel precursor solution on them. By adjusting the B-γ-CsSnI₃ grain crystallization and optimizing the device structure, a photovoltaic conversion efficiency of up to 3.31% was obtained

without any additives, corresponding to an open-circuit voltage of 520 mV, a short-circuit current density of 10.21 mA/cm² and a fill factor of 62.50% (Figure 21c,d, Table 3). The work function of the prepared NiOx layer is about −4.80 eV (Figure 21b), making the energy level of NiOx layer well-matched with that of the B- γ -CsSnI₃ perovskite film and favorable for the hole carrier transport.

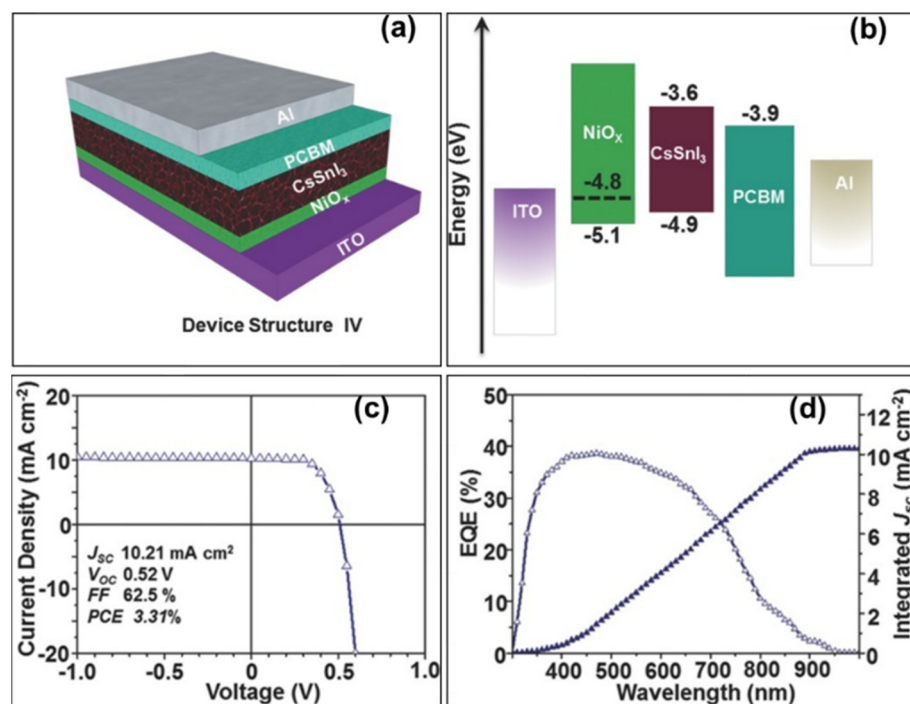


Figure 21. (a) Schematic diagram of the CsSnI₃ device structure using NiOx as the hole transport layer. (b) Device energy level diagram (dashed lines indicate NiOx work function). (c) Current density–voltage diagram of the CsSnI₃ device. (d) Corresponding external quantum efficiency spectra [40]. Reprinted with permission from Ref. [39]. Copyright 2016 John Wiley and Sons.

Table 3. Performance parameters of tin-based perovskite solar cells based on NiOx and CuSCN as hole transport layer.

Perovskite	Device Structure	Voc (mV)	Jsc (mA/cm ²)	FF (%)	PCE (%)	Ref.
B- γ -CsSnI ₃	ITO/NiOx/PVSK/PCBM/Al	520	10.21	62.50	3.31	[40]
2D(PEA ₂ FASn ₂ I ₇)/3D(FASnI ₃)	ITO/NiOx/PVSK/PCBM/BCP/Ag	610	22.00	70.10	9.41	[102]
FASnI ₃	ITO/NiOx/WSe ₂ /PVSK/PCBM/BCP/Ag	630	22.71	73.20	10.47	[103]
FASnI ₃ (5 mol% AHP)	ITO/CuSCN/FASnI ₃ /PCBM/Ag	550	19.39	68.80	7.34	[104]

With NiOx as the hole transport layer, and with 2D/3D structured PEA₂FASn₂I₇ perovskite material as the light absorb layer, Wang et al. prepared devices with the structure of ITO/NiOx/Sn-PVSK/PCBM/BCP/Ag [102]. The valence band of 2D/3D perovskite matches well with that of NiOx, and the conduction band bottom is higher than that of [6,6]-phenyl-C61-butyric acid methyl ester, which allows the carriers to efficiently act as transporters. The hole transport layer precursor solution was obtained by dissolving NiOx nanocrystals in a mixed solution (deionized water: isopropanol 3:1, *v/v*) and filtering with 0.22 μ m polytetrafluoroethylene (PTFE). Finally, the 5% NH₄SCN-doped perovskite solar cells showed the highest power conversion efficiency of 9.41% under AM 1.5G light illumination, corresponding to a current density of 22 mA/cm², an open-circuit voltage of 610 mV and a fill factor of 70.10% (Figure 22a, Table 3). The short-circuit current density value (20.80 mA/cm²) from the external quantum efficiency curve agrees well with the

device short-circuit current density (Figure 22b). Moreover, the histogram of the power efficiency of 45 devices showed excellent reproducibility (Figure 22c). The unencapsulated device in N₂ filled glove box were quite stable for durations up to 600 h (Figure 22d).

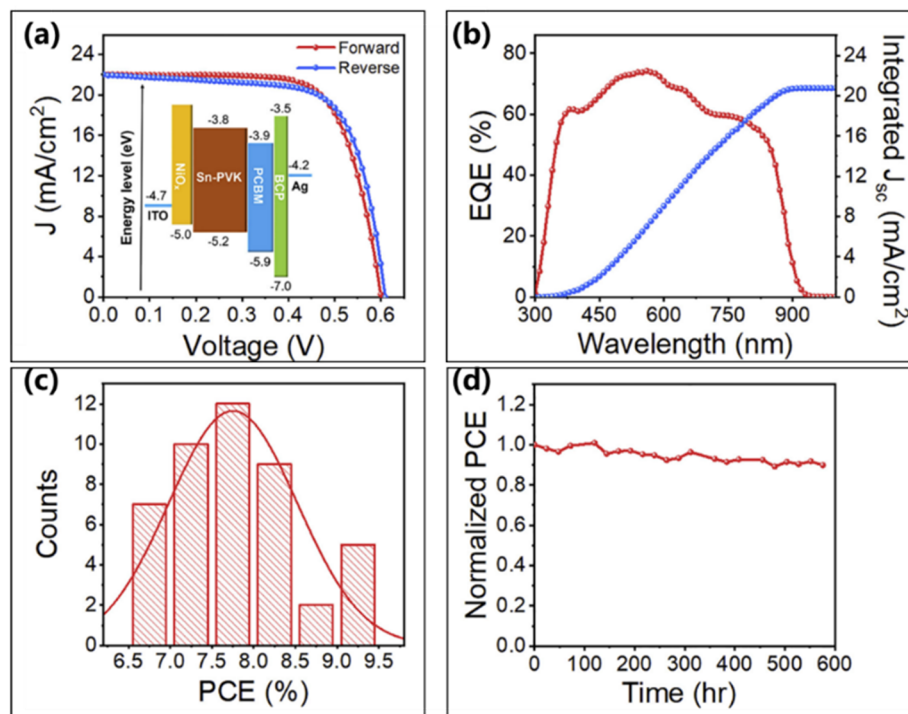


Figure 22. (a) The current density–voltage curves for forward and reverse scan mode devices; the inset shows device energy level diagram. (b) The external quantum efficiency curve of the device. (c) Histogram of the power conversion efficiency of 45 devices. (d) Normalized efficiency curve for devices stored in the N₂ glove box [102]. Reprinted with permission from Ref. [100]. Copyright 2018 Elsevier.

In 2021, Wang et al. prepared tin-based perovskite photovoltaic devices with the structure of ITO/NiOx/WSe₂/FASnI₃/PCBM/BCP/Ag, using NiOx as the hole transport layer, FASnI₃ perovskite material as the light-absorbing layer, and WX₂ flakes as the charge transport interlayer [103]. The device achieved a power conversion efficiency of 10.47%, corresponding to an open-circuit voltage of 630 mV, a short-circuit current density of 22.71 mA/cm², and a fill factor of 73% (Table 3). Compared with NiOx, the WX₂ layer has high hole mobility and higher valence band level, which makes the hole transport layer NiOx/WSe₂ and the perovskite film better matched in energy level and the charge carrier transport more efficient. In summary, NiOx is a type of low-cost hole transport material and can be prepared by physical layer deposition, magnetron sputtering and sol-gel processing; notably, it can be prepared at low temperatures, which provides the possibility of flexible tin perovskite devices. At present, the power conversion efficiency of NiOx-based perovskite device is still low. To further improve the device performance, we need to optimize the preparation of NiOx thin films and improve the light transmission and conductivity of NiOx through reasonable doping.

4.2. Inorganic CuSCN

CuSCN is a type of high hole mobility, high transparent, high stable, and low-cost hole transport layer. Moreover, it has a well-matched energy level with FASnI₃ perovskite (CuSCN: −5.30 eV; FASnI₃: −5.02 eV; Figure 23a). With CuSCN as the hole transport layer, and with NH₄H₂PO₂(AHP)-doped FASnI₃ perovskite as the light absorbing layer, Cao et al. prepared ITO/CuSCN/FASnI₃/PCBM/Ag structure devices [104]. The CuSCN

was dissolved in ammonia (10 mg/mL) and applied via spin-coating on top of the ITO substrate (Figure 23a). The AHP additive introduced in the perovskite solution reduced the oxidation of Sn^{2+} to Sn^{4+} , improved the film morphology, reduced the trap density, and optimized the energy matching between the hole transport layer and the perovskite layer. The final champion device (5 mol% AHP) achieved a power conversion efficiency of 7.34%, corresponding to a short-circuit current of 19.39 mA/cm^2 , an open-circuit voltage of 550 mV and a fill factor of 68.8% (Figure 23b,c, Table 3). In addition, these devices exhibited good long-term stability in both pure nitrogen and ambient air (Figure 23d). Notably, the open-circuit voltage reached up to 550 mV, which was one of the highest values for FASnI_3 -based devices. This was attributed to the reduced defect density in the FASnI_3 films and the effective energy alignment between FASnI_3 and CuSCN .

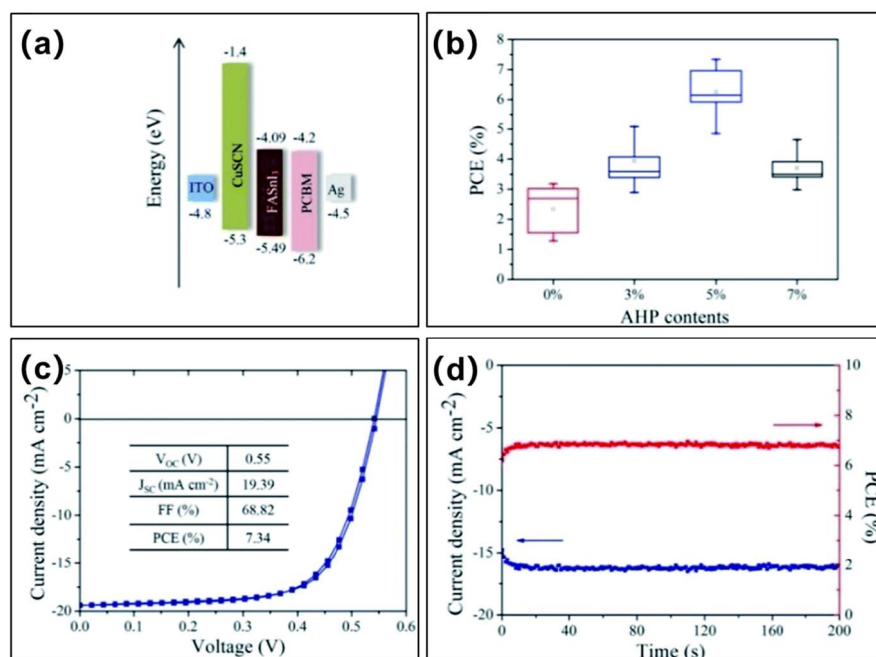


Figure 23. (a) Energy level diagram of the devices. (b) Distribution of power conversion efficiency of devices prepared with different AHP doping. (c) Current density–voltage curves of the champion performance devices. (d) Stable power efficiency and photocurrent density of the devices measured at a bias voltage of 430 mV [104]. Reprinted with permission from Ref. [102]. Copyright 2019 The Royal Society of Chemistry.

5. Conclusions

Although the efficiency of tin-based perovskite solar cells has exceeded 14%, there is still an urgent need to improve device efficiency and stability. In this work, we summarized and analyzed the progress of tin-based perovskite solar cells in recent years, especially from the perspective of the hole transport layer. The efficient and stable tin-based perovskite solar cells were obtained via improvement of the components, structure and additives of the hole transport layer. In selecting an appropriate hole transport material, the chosen material requires an excellent ability to extract holes from the perovskite layer as well as its own hole transport ability, which are mainly based on the following two points: the energy levels between the perovskite layer and the hole transport layer should be well matched; the maintenance of proper contact between the hole transport layer and the perovskite interface, which greatly affect the reproducibility and stability of the device. The current high-efficiency tin-based perovskite solar cells commonly utilize PEDOT:PSS as the hole transport material; however, the hydrophilicity and acidity of PEDOT:PSS are damaging to device stability, thus necessitating further optimization of the PEDOT:PSS layer. Finally, the band gap of tin-based perovskite materials can reach the ideal Shockley–Queisser

equilibrium limit theory (1.34 eV), and tin is an environmentally heavy metal element. Therefore, the research of tin-based perovskite photovoltaic technology would have an important place in solar cell development, and the attention of researchers to the hole transport layer will continue to increase.

Author Contributions: X.C., writing—original draft preparation; J.C. and J.L. supervision; L.H., L.Z. and C.Z. writing—review and editing; J.C. and A.P. funding acquisition. All authors have read and agreed to the published version of the manuscript.

Funding: This research was funded by the Natural Science Foundation of China (52002074) and foundation of Huai'an Science and Technology Project (HAB202158).

Institutional Review Board Statement: Not applicable.

Data Availability Statement: Data availability is not applicable to this article as no new data were created or analyzed in this study.

Acknowledgments: Xin Yao Chen would like to thank Xiaoping Zou for the useful discussion.

Conflicts of Interest: The authors declare no conflict of interest.

References

1. Kojima, A.; Teshima, K.; Shirai, Y.; Miyasaka, T. Organometal halide perovskites as visible-light sensitizers for photovoltaic cells. *J. Am. Chem. Soc.* **2009**, *131*, 6050–6051. [\[CrossRef\]](#)
2. Kim, H.-S.; Lee, C.-R.; Im, J.-H.; Lee, K.-B.; Moehl, T.; Marchioro, A.; Moon, S.-J.; Humphry-Baker, R.; Yum, J.-H.; Moser, J.E. Lead iodide perovskite sensitized all-solid-state submicron thin film mesoscopic solar cell with efficiency exceeding 9%. *Sci. Rep.* **2012**, *2*, 591. [\[CrossRef\]](#) [\[PubMed\]](#)
3. Lee, M.M.; Teuscher, J.; Miyasaka, T.; Murakami, T.N.; Snaith, H.J. Efficient hybrid solar cells based on meso-superstructured organometal halide perovskites. *Science* **2012**, *338*, 643–647. [\[CrossRef\]](#)
4. Park, J.; Kim, J.; Yun, H.-S.; Paik, M.J.; Noh, E.; Mun, H.J.; Kim, M.G.; Shin, T.J.; Seok, S.I. Controlled growth of perovskite layers with volatile alkylammonium chlorides. *Nature* **2023**. [\[CrossRef\]](#)
5. Im, J.-H.; Lee, C.-R.; Lee, J.-W.; Park, S.-W.; Park, N.-G. 6.5% efficient perovskite quantum-dot-sensitized solar cell. *Nanoscale* **2011**, *3*, 4088–4093. [\[CrossRef\]](#) [\[PubMed\]](#)
6. Etgar, L.; Gao, P.; Xue, Z.; Peng, Q.; Chandiran, A.K.; Liu, B.; Nazeeruddin, M.K.; Grätzel, M. Mesoscopic $\text{CH}_3\text{NH}_3\text{PbI}_3/\text{TiO}_2$ Heterojunction Solar Cells. *J. Am. Chem. Soc.* **2012**, *134*, 17396–17399. [\[CrossRef\]](#)
7. Heo, J.H.; Im, S.H.; Noh, J.H.; Mandal, T.N.; Lim, C.-S.; Chang, J.A.; Lee, Y.H.; Kim, H.-J.; Sarkar, A.; Nazeeruddin, M.K.; et al. Efficient inorganic–organic hybrid heterojunction solar cells containing perovskite compound and polymeric hole conductors. *Nat. Photonics* **2013**, *7*, 486–491. [\[CrossRef\]](#)
8. Burschka, J.; Pellet, N.; Moon, S.J.; Humphry-Baker, R.; Gao, P.; Nazeeruddin, M.K.; Grätzel, M. Sequential deposition as a route to high-performance perovskite-sensitized solar cells. *Nature* **2013**, *499*, 316–319. [\[CrossRef\]](#)
9. Liu, M.; Johnston, M.B.; Snaith, H.J. Efficient planar heterojunction perovskite solar cells by vapour deposition. *Nature* **2013**, *501*, 395–398. [\[CrossRef\]](#)
10. Chen, Q.; Zhou, H.; Hong, Z.; Luo, S.; Duan, H.-S.; Wang, H.-H.; Liu, Y.; Li, G.; Yang, Y. Planar Heterojunction Perovskite Solar Cells via Vapor-Assisted Solution Process. *J. Am. Chem. Soc.* **2014**, *136*, 622–625. [\[CrossRef\]](#)
11. Zhou, H.; Chen, Q.; Li, G.; Luo, S.; Song, T.-B.; Duan, H.-S.; Hong, Z.; You, J.; Liu, Y.; Yang, Y. Interface engineering of highly efficient perovskite solar cells. *Science* **2014**, *345*, 542–546. [\[CrossRef\]](#) [\[PubMed\]](#)
12. Yang, W.S.; Noh, J.H.; Jeon, N.J.; Kim, Y.C.; Ryu, S.; Seo, J.; Seok, S.I. High-performance photovoltaic perovskite layers fabricated through intramolecular exchange. *Science* **2015**, *348*, 1234–1237. [\[CrossRef\]](#) [\[PubMed\]](#)
13. Saliba, M.; Matsui, T.; Domanski, K.; Seo, J.Y.; Ummadisingu, A.; Zakeeruddin, S.M.; Correa-Baena, J.-P.; Tress, W.R.; Abate, A.; Hagfeldt, A.; et al. Incorporation of rubidium cations into perovskite solar cells improves photovoltaic performance. *Science* **2016**, *354*, 206–209. [\[CrossRef\]](#) [\[PubMed\]](#)
14. Jeon, N.J.; Na, H.; Jung, E.H.; Yang, T.-Y.; Lee, Y.G.; Kim, G.; Shin, H.-W.; Il Seok, S.; Lee, J.; Seo, J. A fluorene-terminated hole-transporting material for highly efficient and stable perovskite solar cells. *Nat. Energy* **2018**, *3*, 682–689. [\[CrossRef\]](#)
15. Yoo, J.J.; Seo, G.; Chua, M.R.; Park, T.G.; Lu, Y.; Rotermund, F.; Kim, Y.-K.; Moon, C.S.; Jeon, N.J.; Correa-Baena, J.-P.; et al. Efficient perovskite solar cells via improved carrier management. *Nature* **2021**, *590*, 587–593. [\[CrossRef\]](#) [\[PubMed\]](#)
16. Hailegnaw, B.; Kirmayer, S.; Edri, E.; Hodes, G.; Cahen, D. Rain on methylammonium lead iodide based perovskites: Possible environmental effects of perovskite solar cells. *J. Phys. Chem. Lett.* **2015**, *6*, 1543–1547. [\[CrossRef\]](#)
17. Li, J.; Cao, H.-L.; Jiao, W.-B.; Wang, Q.; Wei, M.; Cantone, I.; Lü, J.; Abate, A. Biological impact of lead from halide perovskites reveals the risk of introducing a safe threshold. *Nat. Commun.* **2020**, *11*, 310. [\[CrossRef\]](#) [\[PubMed\]](#)
18. Popov, A.I.; Kotomin, E.A.; Maier, J. Analysis of self-trapped hole mobility in alkali halides and metal halides. *Solid State Ion.* **2017**, *302*, 3–6. [\[CrossRef\]](#)

19. Pazoki, M.; Jacobsson, T.J.; Kullgren, J.; Johansson, E.M.J.; Hagfeldt, A.; Boschloo, G.; Edvinsson, T. Photoinduced Stark Effects and Mechanism of Ion Displacement in Perovskite Solar Cell Materials. *ACS Nano* **2017**, *11*, 2823–2834. [\[CrossRef\]](#)
20. Rusevich, L.L.; Kotomin, E.A.; Zvejnicks, G.; Popov, A.I. Ab initio calculations of structural, electronic and vibrational properties of BaTiO₃ and SrTiO₃ perovskite crystals with oxygen vacancies. *Low Temp. Phys.* **2020**, *46*, 1185–1195. [\[CrossRef\]](#)
21. Even, J.; Pedesseau, L.; Jancu, J.M.; Katan, C. DFT and $k \cdot p$ modelling of the phase transitions of lead and tin halide perovskites for photovoltaic cells. *Phys. Status Solidi (RRL)—Rapid Res. Lett.* **2014**, *8*, 31–35. [\[CrossRef\]](#)
22. Abate, A. Perovskite Solar Cells Go Lead Free. *Joule* **2017**, *1*, 659–664. [\[CrossRef\]](#)
23. Kaiser, W.; Ricciarelli, D.; Mosconi, E.; Althman, A.A.; Ambrosio, F.; De Angelis, F. Stability of Tin- versus Lead-Halide Perovskites: Ab Initio Molecular Dynamics Simulations of Perovskite/Water Interfaces. *J. Phys. Chem. Lett.* **2022**, *13*, 2321–2329. [\[CrossRef\]](#)
24. Mastrikov, Y.A.; Chuklina, N.G.; Sokolov, M.N.; Popov, A.I.; Gryaznov, D.V.; Kotomin, E.A.; Maier, J. Small radius electron and hole polarons in PbX₂ (X = F, Cl, Br) crystals: A computational study. *J. Mater. Chem. C* **2021**, *9*, 16536–16544. [\[CrossRef\]](#)
25. Noel, N.K.; Stranks, S.D.; Abate, A.; Wehrenfennig, C.; Guarnera, S.; Haghighirad, A.A.; Sadhanala, A.; Eperon, G.E.; Pathak, S.K.; Johnston, M.B.; et al. Lead-free organic-inorganic tin halide perovskites for photovoltaic applications. *Energy Environ. Sci.* **2014**, *7*, 3061–3068. [\[CrossRef\]](#)
26. Hao, F.; Stoumpos, C.C.; Cao, D.H.; Chang, R.P.H.; Kanatzidis, M.G. Lead-free solid-state organic-inorganic halide perovskite solar cells. *Nat. Photonics* **2014**, *8*, 489–494. [\[CrossRef\]](#)
27. Liao, Y.; Liu, H.; Zhou, W.; Yang, D.; Shang, Y.; Shi, Z.; Li, B.; Jiang, X.; Zhang, L.; Quan, L.N. Highly oriented low-dimensional tin halide perovskites with enhanced stability and photovoltaic performance. *J. Am. Chem. Soc.* **2017**, *139*, 6693–6699. [\[CrossRef\]](#)
28. Jiang, X.Y.; Li, H.S.; Zhou, Q.L.; Wei, Q.; Wei, M.Y.; Jiang, L.Z.; Wang, Z.; Peng, Z.J.; Wang, F.; Zang, Z.H.; et al. One-Step Synthesis of SnI₂ center dot(DMSO)(x) Adducts for High-Performance Tin Perovskite Solar Cells. *J. Am. Chem. Soc.* **2021**, *143*, 10970–10976. [\[CrossRef\]](#)
29. Ren, G.; Han, W.; Deng, Y.; Wu, W.; Li, Z.; Guo, J.; Bao, H.; Liu, C.; Guo, W. Strategies of modifying spiro-OMeTAD materials for perovskite solar cells: A review. *J. Mater. Chem. A* **2021**, *9*, 4589–4625. [\[CrossRef\]](#)
30. Green, M.A.; Ho-Baillie, A.; Snaith, H.J. The emergence of perovskite solar cells. *Nat. Photonics* **2014**, *8*, 506–514. [\[CrossRef\]](#)
31. Bi, D.Q.; Yi, C.Y.; Luo, J.S.; Decoppet, J.D.; Zhang, F.; Zakeeruddin, S.M.; Li, X.; Hagfeldt, A.; Gratzel, M. Polymer-templated nucleation and crystal growth of perovskite films for solar cells with efficiency greater than 21%. *Nat. Energy* **2016**, *1*, 16142. [\[CrossRef\]](#)
32. Jiang, Q.; Chu, Z.N.; Wang, P.Y.; Yang, X.L.; Liu, H.; Wang, Y.; Yin, Z.G.; Wu, J.L.; Zhang, X.W.; You, J.B. Planar-Structure Perovskite Solar Cells with Efficiency beyond 21%. *Adv. Mater.* **2017**, *29*, 1703852. [\[CrossRef\]](#)
33. Yang, W.S.; Park, B.W.; Jung, E.H.; Jeon, N.J.; Kim, Y.C.; Lee, D.U.; Shin, S.S.; Seo, J.; Kim, E.K.; Noh, J.H.; et al. Iodide management in formamidinium-lead-halide-based perovskite layers for efficient solar cells. *Science* **2017**, *356*, 1376–1379. [\[CrossRef\]](#)
34. Jiang, Q.; Zhao, Y.; Zhang, X.W.; Yang, X.L.; Chen, Y.; Chu, Z.M.; Ye, Q.F.; Li, X.X.; Yin, Z.G.; You, J.B. Surface passivation of perovskite film for efficient solar cells. *Nat. Photonics* **2019**, *13*, 460–466. [\[CrossRef\]](#)
35. Kim, M.; Kim, G.H.; Lee, T.K.; Choi, I.W.; Choi, H.W.; Jo, Y.; Yoon, Y.J.; Kim, J.W.; Lee, J.; Huh, D.; et al. Methylammonium Chloride Induces Intermediate Phase Stabilization for Efficient Perovskite Solar Cells. *Joule* **2019**, *3*, 2179–2192. [\[CrossRef\]](#)
36. Kim, G.; Min, H.; Lee, K.S.; Lee, D.Y.; Yoon, S.M.; Seok, S.I. Impact of strain relaxation on performance of alpha-formamidinium lead iodide perovskite solar cells. *Science* **2020**, *370*, 108–112. [\[CrossRef\]](#) [\[PubMed\]](#)
37. Min, H.; Lee, D.Y.; Kim, J.; Kim, G.; Lee, K.S.; Kim, J.; Paik, M.J.; Kim, Y.K.; Kim, K.S.; Kim, M.G.; et al. Perovskite solar cells with atomically coherent interlayers on SnO₂ electrodes. *Nature* **2021**, *598*, 444–450. [\[CrossRef\]](#) [\[PubMed\]](#)
38. Zhu, G.; Yang, L.; Zhang, C.; Du, G.; Fan, N.; Luo, Z.; Zhang, X.; Zhang, J. Unveiling the Critical Role of Oxidants and Additives in Doped Spiro-OMeTAD toward Stable and Efficient Perovskite Solar Cells. *ACS Appl. Energy Mater.* **2022**, *5*, 3595–3604. [\[CrossRef\]](#)
39. Kong, J.; Shin, Y.; Röhr, J.A.; Wang, H.; Meng, J.; Wu, Y.; Katzenberg, A.; Kim, G.; Kim, D.Y.; Li, T.-D.; et al. CO₂ doping of organic interlayers for perovskite solar cells. *Nature* **2021**, *594*, 51–56. [\[CrossRef\]](#)
40. Wang, N.; Zhou, Y.Y.; Ju, M.G.; Garces, H.F.; Ding, T.; Pang, S.P.; Zeng, X.C.; Padture, N.P.; Sun, X.W. Heterojunction-Depleted Lead-Free Perovskite Solar Cells with Coarse-Grained B-gamma-CsSnI₃ Thin Films. *Adv. Energy Mater.* **2016**, *6*, 1601130. [\[CrossRef\]](#)
41. Ke, W.J.; Priyanka, P.; Vegiraju, S.; Stoumpos, C.C.; Spanopoulos, I.; Soe, C.M.M.; Marks, T.J.; Chen, M.C.; Kanatzidis, M.G. Dopant-Free Tetrakis-Triphenylamine Hole Transporting Material for Efficient Tin-Based Perovskite Solar Cells. *J. Am. Chem. Soc.* **2018**, *140*, 388–393. [\[CrossRef\]](#) [\[PubMed\]](#)
42. Kumar, M.H.; Dharani, S.; Leong, W.L.; Boix, P.P.; Prabhakar, R.R.; Baikie, T.; Shi, C.; Ding, H.; Ramesh, R.; Asta, M.; et al. Lead-Free Halide Perovskite Solar Cells with High Photocurrents Realized Through Vacancy Modulation. *Adv. Mater.* **2014**, *26*, 7122–7127. [\[CrossRef\]](#)
43. Gupta, S.; Bendikov, T.; Hodes, G.; Cahen, D. CsSnBr₃, A Lead-Free Halide Perovskite for Long-Term Solar Cell Application: Insights on SnF₂ Addition. *ACS Energy Lett.* **2016**, *1*, 1028–1033. [\[CrossRef\]](#)
44. Koh, T.M.; Krishnamoorthy, T.; Yantara, N.; Shi, C.; Leong, W.L.; Boix, P.P.; Grimsdale, A.C.; Mhaisalkar, S.G.; Mathews, N. Formamidinium tin-based perovskite with low E-g for photovoltaic applications. *J. Mater. Chem. A* **2015**, *3*, 14996–15000. [\[CrossRef\]](#)

45. Jung, M.-C.; Raga, S.R.; Qi, Y. Properties and solar cell applications of Pb-free perovskite films formed by vapor deposition. *RSC Adv.* **2016**, *6*, 2819–2825. [\[CrossRef\]](#)
46. Lee, S.J.; Shin, S.S.; Im, J.; Ahn, T.K.; Noh, J.H.; Jeon, N.J.; Seok, S.I.; Seo, J. Reducing Carrier Density in Formamidinium Tin Perovskites and Its Beneficial Effects on Stability and Efficiency of Perovskite Solar Cells. *ACS Energy Lett.* **2018**, *3*, 46–53. [\[CrossRef\]](#)
47. Yokoyama, T.; Cao, D.H.; Stoumpos, C.C.; Song, T.B.; Sato, Y.; Aramaki, S.; Kanatzidis, M.G. Overcoming Short-Circuit in Lead-Free $\text{CH}_3\text{NH}_3\text{SnI}_3$ Perovskite Solar Cells via Kinetically Controlled Gas-Solid Reaction Film Fabrication Process. *J. Phys. Chem. Lett.* **2016**, *7*, 776–782. [\[CrossRef\]](#) [\[PubMed\]](#)
48. Xia, J.; Zhang, Y.; Xiao, C.; Brooks, K.G.; Chen, M.; Luo, J.; Yang, H.; Klipfel, N.I.D.; Zou, J.; Shi, Y.; et al. Tailoring electric dipole of hole-transporting material p-dopants for perovskite solar cells. *Joule* **2022**, *6*, 1689–1709. [\[CrossRef\]](#)
49. Li, F.; Xie, Y.; Hu, Y.; Long, M.; Zhang, Y.; Xu, J.; Qin, M.; Lu, X.; Liu, M. Effects of Alkyl Chain Length on Crystal Growth and Oxidation Process of Two-Dimensional Tin Halide Perovskites. *ACS Energy Lett.* **2020**, *5*, 1422–1429. [\[CrossRef\]](#)
50. Handa, T.; Yamada, T.; Kubota, H.; Ise, S.; Miyamoto, Y.; Kanemitsu, Y. Photocarrier Recombination and Injection Dynamics in Long-Term Stable Lead-Free $\text{CH}_3\text{NH}_3\text{SnI}_3$ Perovskite Thin Films and Solar Cells. *J. Phys. Chem. C* **2017**, *121*, 16158–16165. [\[CrossRef\]](#)
51. Do Kim, H.; Miyamoto, Y.; Kubota, H.; Yamanari, T.; Ohkita, H. Open-circuit Voltage Loss in $\text{CH}_3\text{NH}_3\text{SnI}_3$ Perovskite Solar Cells. *Chem. Lett.* **2017**, *46*, 253–256. [\[CrossRef\]](#)
52. Ke, W.J.; Stoumpos, C.C.; Logsdon, J.L.; Wasielewski, M.R.; Yan, Y.F.; Fang, G.J.; Kanatzidis, M.G. TiO_2 -ZnS Cascade Electron Transport Layer for Efficient Formamidinium Tin Iodide Perovskite Solar Cells. *J. Am. Chem. Soc.* **2016**, *138*, 14998–15003. [\[CrossRef\]](#)
53. Ke, W.; Stoumpos Constantinos, C.; Zhu, M.; Mao, L.; Spanopoulos, I.; Liu, J.; Kontsevoi Oleg, Y.; Chen, M.; Sarma, D.; Zhang, Y.; et al. Enhanced photovoltaic performance and stability with a new type of hollow 3D perovskite $\{\text{en}\}\text{FASnI}_3$. *Sci. Adv.* **2017**, *3*, e1701293. [\[CrossRef\]](#)
54. Cao, D.H.; Stoumpos, C.C.; Yokoyama, T.; Logsdon, J.L.; Song, T.B.; Farha, O.K.; Wasielewski, M.R.; Hupp, J.T.; Kanatzidis, M.G. Thin Films and Solar Cells Based on Semiconducting Two-Dimensional Ruddlesden-Popper $(\text{CH}_3(\text{CH}_2)_3\text{NH}_3)_2(\text{CH}_3\text{NH}_3)_{n-1}\text{Sn}_n\text{I}_{3n+1}$ Perovskites. *ACS Energy Lett.* **2017**, *2*, 982–990. [\[CrossRef\]](#)
55. Ke, W.J.; Stoumpos, C.C.; Spanopoulos, I.; Mao, L.; Chen, M.; Wasielewski, M.R.; Kanatzidis, M.G. Efficient Lead-Free Solar Cells Based on Hollow $\{\text{en}\}\text{MASnI}_3$ Perovskites. *J. Am. Chem. Soc.* **2017**, *139*, 14800–14806. [\[CrossRef\]](#)
56. Song, T.B.; Yokoyama, T.; Stoumpos, C.C.; Logsdon, J.; Cao, D.H.; Wasielewski, M.R.; Aramaki, S.; Kanatzidis, M.G. Importance of Reducing Vapor Atmosphere in the Fabrication of Tin-Based Perovskite Solar Cells. *J. Am. Chem. Soc.* **2017**, *139*, 836–842. [\[CrossRef\]](#) [\[PubMed\]](#)
57. Ke, W.; Stoumpos, C.C.; Spanopoulos, I.; Chen, M.; Wasielewski, M.R.; Kanatzidis, M.G. Diammonium Cations in the FASnI_3 Perovskite Structure Lead to Lower Dark Currents and More Efficient Solar Cells. *ACS Energy Lett.* **2018**, *3*, 1470–1476. [\[CrossRef\]](#)
58. Yang, Z.; Zhong, M.; Liang, Y.; Yang, L.; Liu, X.; Li, Q.; Zhang, J.; Xu, D. SnO_2 -C₆₀ Pyrrolidine Tris-Acid (CPTA) as the Electron Transport Layer for Highly Efficient and Stable Planar Sn-Based Perovskite Solar Cells. *Adv. Funct. Mater.* **2019**, *29*, 1903621. [\[CrossRef\]](#)
59. Qiu, X.F.; Jiang, Y.A.; Zhang, H.L.; Qiu, Z.W.; Yuan, S.; Wang, P.; Cao, B.Q. Lead-free mesoscopic Cs_2SnI_6 perovskite solar cells using different nanostructured ZnO nanorods as electron transport layers. *Phys. Status Solidi-Rapid Res. Lett.* **2016**, *10*, 587–591. [\[CrossRef\]](#)
60. Qiu, X.F.; Cao, B.Q.; Yuan, S.; Chen, X.F.; Qiu, Z.W.; Jiang, Y.A.; Ye, Q.; Wang, H.Q.; Zeng, H.B.; Liu, J.; et al. From unstable CsSnI_3 to air-stable Cs_2SnI_6 : A lead-free perovskite solar cell light absorber with bandgap of 1.48 eV and high absorption coefficient. *Sol. Energy Mater. Sol. Cells* **2017**, *159*, 227–234. [\[CrossRef\]](#)
61. Liao, W.Q.; Zhao, D.W.; Yu, Y.; Grice, C.R.; Wang, C.L.; Cimaroli, A.J.; Schulz, P.; Meng, W.W.; Zhu, K.; Xiong, R.G.; et al. Lead-Free Inverted Planar Formamidinium Tin Triiodide Perovskite Solar Cells Achieving Power Conversion Efficiencies up to 6.22%. *Adv. Mater.* **2016**, *28*, 9333–9340. [\[CrossRef\]](#)
62. Fujihara, T.; Terakawa, S.; Matsushima, T.; Qin, C.; Yahiro, M.; Adachi, C. Fabrication of high coverage MASnI_3 perovskite films for stable, planar heterojunction solar cells. *J. Mater. Chem. C* **2017**, *5*, 1121–1127. [\[CrossRef\]](#)
63. Xi, J.; Wu, Z.X.; Jiao, B.; Dong, H.; Ran, C.X.; Piao, C.C.; Lei, T.; Song, T.B.; Ke, W.J.; Yokoyama, T.; et al. Multichannel Interdiffusion Driven FASnI_3 Film Formation Using Aqueous Hybrid Salt/Polymer Solutions toward Flexible Lead-Free Perovskite Solar Cells. *Adv. Mater.* **2017**, *29*, 1606964. [\[CrossRef\]](#) [\[PubMed\]](#)
64. Zhao, Z.R.; Gu, F.D.; Li, Y.L.; Sun, W.H.; Ye, S.Y.; Rao, H.X.; Liu, Z.W.; Bian, Z.Q.; Huang, C.H. Mixed-Organic-Cation Tin Iodide for Lead-Free Perovskite Solar Cells with an Efficiency of 8.12%. *Adv. Sci.* **2017**, *4*, 1700204. [\[CrossRef\]](#) [\[PubMed\]](#)
65. Chen, K.; Wu, P.; Yang, W.Q.; Su, R.; Luo, D.Y.; Yang, X.Y.; Tu, Y.G.; Zhu, R.; Gong, Q.H. Low-dimensional perovskite interlayer for highly efficient lead-free formamidinium tin iodide perovskite solar cells. *Nano Energy* **2018**, *49*, 411–418. [\[CrossRef\]](#)
66. Deng, L.; Wang, K.; Yang, H.; Yu, H.; Hu, B. Polymer assist crystallization and passivation for enhancements of open-circuit voltage and stability in tin-halide perovskite solar cells. *J. Phys. D Appl. Phys.* **2018**, *51*, 475102. [\[CrossRef\]](#)
67. Kayesh, M.E.; Chowdhury, T.H.; Matsuishi, K.; Kaneko, R.; Kazaoui, S.; Lee, J.-J.; Noda, T.; Islam, A. Enhanced Photovoltaic Performance of FASnI_3 -Based Perovskite Solar Cells with Hydrazinium Chloride Coadditive. *ACS Energy Lett.* **2018**, *3*, 1584–1589. [\[CrossRef\]](#)

68. Kim, H.; Lee, Y.H.; Lyu, T.; Yoo, J.H.; Park, T.; Oh, J.H. Boosting the performance and stability of quasi-two-dimensional tin-based perovskite solar cells using the formamidinium thiocyanate additive. *J. Mater. Chem. A* **2018**, *6*, 18173–18182. [\[CrossRef\]](#)
69. Shao, S.Y.; Liu, J.; Portale, G.; Fang, H.H.; Blake, G.R.; ten Brink, G.H.; Koster, L.J.A.; Loi, M.A. Highly Reproducible Sn-Based Hybrid Perovskite Solar Cells with 9% Efficiency. *Adv. Energy Mater.* **2018**, *8*, 170201. [\[CrossRef\]](#)
70. Zhu, Z.L.; Chueh, C.C.; Li, N.; Mao, C.Y.; Jen, A.K.Y. Realizing Efficient Lead-Free Formamidinium Tin Triiodide Perovskite Solar Cells via a Sequential Deposition Route. *Adv. Mater.* **2018**, *30*, 1703800. [\[CrossRef\]](#)
71. Jokar, E.; Chien, C.-H.; Tsai, C.-M.; Fathi, A.; Diau, E.W.-G. Robust Tin-Based Perovskite Solar Cells with Hybrid Organic Cations to Attain Efficiency Approaching 10%. *Adv. Mater.* **2019**, *31*, 1804835. [\[CrossRef\]](#)
72. Kamarudin, M.A.; Hirotani, D.; Wang, Z.; Hamada, K.; Nishimura, K.; Shen, Q.; Toyoda, T.; Iikubo, S.; Minemoto, T.; Yoshino, K.; et al. Suppression of Charge Carrier Recombination in Lead-Free Tin Halide Perovskite via Lewis Base Post-treatment. *J. Phys. Chem. Lett.* **2019**, *10*, 5277–5283. [\[CrossRef\]](#)
73. Kayesh, M.E.; Matsuishi, K.; Kaneko, R.; Kazaoui, S.; Lee, J.J.; Noda, T.; Islam, A. Coadditive Engineering with 5-Ammonium Valeric Acid Iodide for Efficient and Stable Sn Perovskite Solar Cells. *ACS Energy Lett.* **2019**, *4*, 278–284. [\[CrossRef\]](#)
74. Liao, M.; Yu, B.B.; Jin, Z.X.; Chen, W.; Zhu, Y.D.; Zhang, X.S.; Yao, W.T.; Duan, T.; Djerdj, I.; He, Z.B. Efficient and Stable FASnI₃ Perovskite Solar Cells with Effective Interface Modulation by Low-Dimensional Perovskite Layer. *Chemsuschem* **2019**, *12*, 5007–5014. [\[CrossRef\]](#)
75. Nishimura, K.; Hirotani, D.; Kamarudin, M.A.; Shen, Q.; Toyoda, T.; Iikubo, S.; Minemoto, T.; Yoshino, K.; Hayase, S. Relationship between Lattice Strain and Efficiency for Sn-Perovskite Solar Cells. *ACS Appl. Mater. Interfaces* **2019**, *11*, 31105–31110. [\[CrossRef\]](#)
76. Qiu, J.; Xia, Y.D.; Zheng, Y.T.; Hui, W.; Gu, H.; Yuan, W.B.; Yu, H.; Chao, L.F.; Niu, T.T.; Yang, Y.G.; et al. 2D Intermediate Suppression for Efficient Ruddlesden-Popper (RP) Phase Lead-Free Perovskite Solar Cells. *ACS Energy Lett.* **2019**, *4*, 1513–1520. [\[CrossRef\]](#)
77. Ran, C.X.; Gao, W.Y.; Li, J.R.; Xi, J.; Li, L.; Dai, J.F.; Yang, Y.G.; Gao, X.Y.; Dong, H.; Jiao, B.; et al. Conjugated Organic Cations Enable Efficient Self-Healing FASnI₃ Solar Cells. *Joule* **2019**, *3*, 3072–3087. [\[CrossRef\]](#)
78. Shao, S.Y.; Dong, J.J.; Duim, H.; ten Brink, G.H.; Blake, G.R.; Portale, G.; Loi, M.A. Enhancing the crystallinity and perfecting the orientation of formamidinium tin iodide for highly efficient Sn-based perovskite solar cells. *Nano Energy* **2019**, *60*, 810–816. [\[CrossRef\]](#)
79. Xu, H.Y.; Jiang, Y.Z.; He, T.W.; Li, S.S.; Wang, H.H.; Chen, Y.; Yuan, M.J.; Chen, J. Orientation Regulation of Tin-Based Reduced-Dimensional Perovskites for Highly Efficient and Stable Photovoltaics. *Adv. Funct. Mater.* **2019**, *29*, 1807696. [\[CrossRef\]](#)
80. Jiang, X.; Wang, F.; Wei, Q.; Li, H.; Shang, Y.; Zhou, W.; Wang, C.; Cheng, P.; Chen, Q.; Chen, L.; et al. Ultra-high open-circuit voltage of tin perovskite solar cells via an electron transporting layer design. *Nat. Commun.* **2020**, *11*, 1245. [\[CrossRef\]](#) [\[PubMed\]](#)
81. Lee, M.; Kim, D.; Lee, Y.K.; Koo, H.; Lee, K.T.; Chung, I. Indene-C60 Bisadduct Electron-Transporting Material with the High LUMO Level Enhances Open-Circuit Voltage and Efficiency of Tin-Based Perovskite Solar Cells. *ACS Appl. Energy Mater.* **2020**, *3*, 5581–5588. [\[CrossRef\]](#)
82. Meng, X.Y.; Wu, T.H.; Liu, X.; He, X.; Noda, T.; Wang, Y.B.; Segawa, H.; Han, L.Y. Highly Reproducible and Efficient FASnI₃ Perovskite Solar Cells Fabricated with Volatilizable Reducing Solvent. *J. Phys. Chem. Lett.* **2020**, *11*, 2965–2971. [\[CrossRef\]](#) [\[PubMed\]](#)
83. Nishimura, K.; Kamarudin, M.A.; Hirotani, D.; Hamada, K.; Shen, Q.; Iikubo, S.; Minemoto, T.; Yoshino, K.; Hayase, S. Lead-free tin-halide perovskite solar cells with 13% efficiency. *Nano Energy* **2020**, *74*, 104858. [\[CrossRef\]](#)
84. Wang, C.B.; Gu, F.D.; Zhao, Z.R.; Rao, H.X.; Qiu, Y.M.; Cai, Z.L.; Zhan, G.; Li, X.Y.; Sun, B.X.; Yu, X.; et al. Self-Repairing Tin-Based Perovskite Solar Cells with a Breakthrough Efficiency Over 11%. *Adv. Mater.* **2020**, *32*, 1907623. [\[CrossRef\]](#) [\[PubMed\]](#)
85. Jokar, E.; Cheng, P.Y.; Lin, C.Y.; Narra, S.; Shahbazi, S.; Diau, E.W.G. Enhanced Performance and Stability of 3D/2D Tin Perovskite Solar Cells Fabricated with a Sequential Solution Deposition. *ACS Energy Lett.* **2021**, *6*, 485–492. [\[CrossRef\]](#)
86. Li, B.; Di, H.; Chang, B.; Yin, R.; Fu, L.; Zhang, Y.-N.; Yin, L. Efficient Passivation Strategy on Sn Related Defects for High Performance All-Inorganic CsSnI₃ Perovskite Solar Cells. *Adv. Funct. Mater.* **2021**, *31*, 2007447. [\[CrossRef\]](#)
87. Wang, C.B.; Zhang, Y.T.; Gu, F.D.; Zhao, Z.R.; Li, H.S.; Jiang, H.; Bian, Z.Q.; Liu, Z.W. Illumination Durability and High-Efficiency Sn-Based Perovskite Solar Cell under Coordinated Control of Phenylhydrazine and Halogen Ions. *Matter* **2021**, *4*, 709–721. [\[CrossRef\]](#)
88. Yu, B.-B.; Chen, Z.; Zhu, Y.; Wang, Y.; Han, B.; Chen, G.; Zhang, X.; Du, Z.; He, Z. Heterogeneous 2D/3D Tin-Halides Perovskite Solar Cells with Certified Conversion Efficiency Breaking 14%. *Adv. Mater.* **2021**, *33*, 2102055. [\[CrossRef\]](#) [\[PubMed\]](#)
89. Li, H.S.; Zang, Z.H.; Wei, Q.; Jiang, X.Y.; Ma, M.Y.; Xing, Z.S.; Wang, J.T.; Yu, D.N.; Wang, F.; Zhou, W.J.; et al. High-member low-dimensional Sn-based perovskite solar cells. *Sci. China-Chem.* **2023**, *66*, 459–465. [\[CrossRef\]](#)
90. Liu, X.; Wang, Y.B.; Xie, F.X.; Yang, X.D.; Han, L.Y. Improving the Performance of Inverted Formamidinium Tin Iodide Perovskite Solar Cells by Reducing the Energy-Level Mismatch. *ACS Energy Lett.* **2018**, *3*, 1116–1121. [\[CrossRef\]](#)
91. Liu, X.; Wu, T.H.; Chen, J.Y.; Meng, X.Y.; He, X.; Noda, T.; Chen, H.; Yang, X.D.; Segawa, H.; Wang, Y.B.; et al. Templated growth of FASnI₃ crystals for efficient tin perovskite solar cells. *Energy Environ. Sci.* **2020**, *13*, 2896–2902. [\[CrossRef\]](#)
92. Zhao, D.; Sexton, M.; Park, H.-Y.; Baure, G.; Nino, J.C.; So, F. High-Efficiency Solution-Processed Planar Perovskite Solar Cells with a Polymer Hole Transport Layer. *Adv. Energy Mater.* **2015**, *5*, 1401855. [\[CrossRef\]](#)
93. Boehm, A.M.; Liu, T.; Park, S.M.; Abtahi, A.; Graham, K.R. Influence of Surface Ligands on Energetics at FASnI₃/C₆₀ Interfaces and Their Impact on Photovoltaic Performance. *ACS Appl. Mater. Interfaces* **2020**, *12*, 5209–5218. [\[CrossRef\]](#) [\[PubMed\]](#)

94. Dong, J.J.; Shao, S.Y.; Kahmann, S.; Rommens, A.J.; Hermida-Merino, D.; ten Brink, G.H.; Loi, M.A.; Portale, G. Mechanism of Crystal Formation in Ruddlesden-Popper Sn-Based Perovskites. *Adv. Funct. Mater.* **2020**, *30*, 2001294. [[CrossRef](#)]
95. Yu, Y.; Zhao, D.W.; Grice, C.R.; Meng, W.W.; Wang, C.L.; Liao, W.Q.; Cimaroli, A.J.; Zhang, H.M.; Zhu, K.; Yan, Y.F. Thermally evaporated methylammonium tin triiodide thin films for lead-free perovskite solar cell fabrication. *RSC Adv.* **2016**, *6*, 90248–90254. [[CrossRef](#)]
96. Ran, C.X.; Xi, J.; Gao, W.Y.; Yuan, F.; Lei, T.; Jiao, B.; Hou, X.; Wu, Z.X. Bilateral Interface Engineering toward Efficient 2D-3D Bulk Heterojunction Tin Halide Lead-Free Perovskite Solar Cells. *ACS Energy Lett.* **2018**, *3*, 713–721. [[CrossRef](#)]
97. Schulz, P.; Edri, E.; Kirmayer, S.; Hodes, G.; Cahen, D.; Kahn, A. Interface energetics in organo-metal halide perovskite-based photovoltaic cells. *Energy Environ. Sci.* **2014**, *7*, 1377–1381. [[CrossRef](#)]
98. Hou, Y.; Chen, W.; Baran, D.; Stubhan, T.; Luechinger, N.A.; Hartmeier, B.; Richter, M.; Min, J.; Chen, S.; Quiroz, C.O.R.; et al. Overcoming the Interface Losses in Planar Heterojunction Perovskite-Based Solar Cells. *Adv. Mater.* **2016**, *28*, 5112–5120. [[CrossRef](#)]
99. Zuo, C.; Ding, L. Modified PEDOT Layer Makes a 1.52 V Voc for Perovskite/PCBM Solar Cells. *Adv. Energy Mater.* **2017**, *7*, 1601193. [[CrossRef](#)]
100. Wolff, C.M.; Zu, F.; Paulke, A.; Toro, L.P.; Koch, N.; Neher, D. Reduced Interface-Mediated Recombination for High Open-Circuit Voltages in CH₃NH₃PbI₃ Solar Cells. *Adv. Mater.* **2017**, *29*, 1700159. [[CrossRef](#)] [[PubMed](#)]
101. Wu, C.-G.; Chiang, C.-H.; Chang, S.H. A perovskite cell with a record-high-V_{oc} of 1.61 V based on solvent annealed CH₃NH₃PbBr₃/ICBA active layer. *Nanoscale* **2016**, *8*, 4077–4085. [[CrossRef](#)] [[PubMed](#)]
102. Wang, F.; Jiang, X.Y.; Chen, H.; Shang, Y.Q.; Liu, H.F.; Wei, J.L.; Zhou, W.J.; He, H.L.; Liu, W.M.; Ning, Z.J. 2D-Quasi-2D-3D Hierarchy Structure for Tin Perovskite Solar Cells with Enhanced Efficiency and Stability. *Joule* **2018**, *2*, 2732–2743. [[CrossRef](#)]
103. Wang, T.; Zheng, F.; Tang, G.; Cao, J.; You, P.; Zhao, J.; Yan, F. 2D WSe₂ Flakes for Synergistic Modulation of Grain Growth and Charge Transfer in Tin-Based Perovskite Solar Cells. *Adv. Sci.* **2021**, *8*, 2004315. [[CrossRef](#)] [[PubMed](#)]
104. Cao, J.; Tai, Q.; You, P.; Tang, G.; Wang, T.; Wang, N.; Yan, F. Enhanced performance of tin-based perovskite solar cells induced by an ammonium hypophosphite additive. *J. Mater. Chem. A* **2019**, *7*, 26580–26585. [[CrossRef](#)]

Disclaimer/Publisher's Note: The statements, opinions and data contained in all publications are solely those of the individual author(s) and contributor(s) and not of MDPI and/or the editor(s). MDPI and/or the editor(s) disclaim responsibility for any injury to people or property resulting from any ideas, methods, instructions or products referred to in the content.